Available online at www.sciencedirect.com

SCIENCE DIRECT®

Journal of Volcanology and Geothermal Research 135 (2004) 195–219

Journal of volcanology and geothermal research

www.elsevier.com/locate/jvolgeores

Analysis of hot springs and associated deposits in Yellowstone National Park using ASTER and AVIRIS remote sensing

Melanie J. Hellman*, Michael S. Ramsey

Department of Geology and Planetary Science, University of Pittsburgh, Pittsburgh, PA 15260-3332, USA

Accepted 5 December 2003

Abstract

The Advanced Spaceborne Thermal Emission and Reflection Radiometer (ASTER) and the Airborne Visible/IR Image Spectrometer (AVIRIS) data were used to characterize hot spring deposits in the Lower, Midway, and Upper Geyser Basins of Yellowstone National Park from the visible/near infrared (VNIR) to thermal infrared (TIR) wavelengths. Field observations of these basins provided the critical ground-truth for comparison with the remote sensing results. Fourteen study sites were selected based on diversity in size, deposit type, and thermal activity. Field work included detailed site surveys such as land cover analysis, photography, Global Positioning System (GPS) data collection, radiometric analysis, and VNIR spectroscopy. Samples of hot spring deposits, geyser deposits, and soil were also collected. Analysis of ASTER data provided broad scale characteristics of the hot springs and their deposits, including the identification of thermal anomalies. AVIRIS high spectral resolution short-wave infrared (SWIR) spectroscopy provided the ability to detect hydrothermally altered minerals as well as a calibration for the multispectral SWIR ASTER data. From the image analysis, differences in these basins were identified including the extent of thermal alteration, the location and abundance of alteration minerals, and a comparison of active, near-extinct, and extinct geysers. We determined the activity level of each region using a combination of the VNIR-SWIR-TIR spectral differences as well as the presence of elevated temperatures, detected by the TIR subsystem of ASTER. The results of this study are applicable to the exploration of extinct mineralized hydrothermal deposits on both Earth and Mars.

Keywords: remote sensing; instruments and techniques; geothermal systems; Mars

1. Introduction

There are thousands of known thermal springs on Earth, with the most abundant located in volcanic areas, such as the Yellowstone Caldera, New Zealand, and Iceland (Walter and DesMarais, 1993; Bryan, 2000). Thermal spring deposits are produced by intense hydrothermal alteration of the surrounding parent rock. As spring waters cool, solubility rapidly decreases and silica is deposited in springs (Walter and DesMarais, 1993). Sinters, the chemical precipitates of hydrothermal systems, generally consist of minerals dominated by silica, carbonate, metallic sulfides and oxides, and clays (Farmer, 2000).

* Corresponding author. Tel.: +1-412-624-8780; fax: +1-412-624-3914.

E-mail addresses: mjh@si.rr.com (M.J. Hellman).

0377-0273/$ - see front matter © 2004 Elsevier B.V. All rights reserved.
doi:10.1016/j.jvolgeores.2003.12.012

Hydrothermal systems may have been crucial to the early evolution of life' and thermophilic organisms may be the common ancestors to all terrestrial life. The search for extant or extinct life on Mars and other planetary bodies is of major importance to the NASA Astrobiology program (Farmer et al., 2001). By using the Earth as an analogue, researchers suggest that if Martian life developed, it would have been in close association with hydrothermal systems (Farmer and DesMarais, 1999). Finding potential hydrothermal sites is a high priority in Martian exploration, and possible hydrothermal activity has been suggested for numerous sites on Mars (Bulmer and Gregg, 1998; Nelson et al., 1998; Dohm et al., 2000; Gulick, 1998).

Investigators including Christiansen (1984) and Fournier and Pitt (1985) described the geological and geophysical characteristics of Yellowstone. Most of the geyser basins have chloride-rich waters that are neutral to slightly alkaline (Fournier, 1989). Hydrothermal fluids from the basins range in temperature from 180 to 270 °C at depths of 100–550 m (Fournier, 1989). Bargar and Fournier (1988) sampled fluid inclusions in the hydrothermal minerals from within major zones of upflow. The homogenization temperatures (T_h values) of the inclusions were all equal to or greater than presently measured rock temperatures at the point of collection, indicating that the thermal waters have not been cooler than present temperatures since formation of the host minerals. Also, because the presence of glacial ice seems to be required to explain the elevated boiling point curves, they determined that hydrothermal activity has operated at its present level from the end of last glaciation (at least 15 ka). Previous studies have found abundant microfossil evidence in Yellowstone's lower temperature thermal spring deposits (Farmer et al., 1995; Farmer and DesMarais, 1999).

There has also been a renewed interest in Yellowstone's hot springs because of the potential medical applications of thermophilic organisms. For instance, the bacterium *Thermus aquaticus* was discovered in springs near the Great Fountain Geyser of the Lower Geyser Basin (Brock, 1994). The bacteria contain Taq polymerase, an enzyme that has been cultured and is now the basis of a US$300 million industry; the enzyme is widely used in medical diagnosis and forensics to copy and amplify DNA (Brock, 1994).

The present study focuses on extinct to active hot springs and hot spring deposits of the Lower, Midway, and Upper Geyser Basins in Yellowstone. ASTER (Advanced Spaceborne Thermal Emission and Reflection Radiometer) and AVIRIS (Airborne Visible/Infrared Image Spectrometer) data analysis was combined with field mapping of the hydrothermal deposits in order to detect differences in the size, activity, and mineralogy of the deposits (Hellman and Ramsey, 2001; Hellman, 2002). Yellowstone National Park was chosen for this study for several reasons: (1) it has the greatest concentration of geysers and hot springs on Earth; (2) the geyser basins typify the surface expression of a high-temperature hot-water system (Fournier, 1989); (3) the preservation of these thermal features allows for a comprehensive study of their deposits; and (4) the remote sensing data availability was far greater than for other hydrothermal sites. Specifically, the Lower, Midway, and Upper Geyser Basins of Yellowstone National Park were chosen for detailed analyses. The Lower Geyser Basin was selected because it is the largest thermal area in Yellowstone. This large area allows for remote sensing studies using decreased spatial resolutions, which can be advantageous for planetary comparisons. Also, this basin has a diverse variety of active and extinct springs. The Midway Geyser Basin was chosen because it is essentially an extension of the Lower Geyser Basin. The Upper Geyser Basin was selected because it has the largest concentration of geysers in the world, allowing for remote sensing observations of intense thermal activity in a relatively small area.

The primary goal of this study was to compare and contrast the characteristics of Yellowstone's active and extinct hot springs. These characteristics were distinguished using field-based, airborne and spaceborne-based reflectance, emissivity and temperature, and band ratioing. Because remote sensing instruments are commonly used in planetary studies and field-based validation is difficult to impossible for other planetary bodies, this type of terrestrial remote sensing analysis can be useful for planetary comparisons. Potential active or extinct hot springs may be detected on Mars using similar techniques implemented in this study.

2. Remote sensing background

The earliest use of satellite geological remote sensing was for mineral exploration in the 1970s (Vincent, 1997). Abrams et al. (1977) identified hydrothermal alteration minerals in the Cuprite mining district from a NASA airborne multispectral scanner, but could only map altered rocks based on the absence of iron oxide and presence of clay minerals. Several years later, Vincent et al. (1984) implemented multispectral airborne and spaceborne thermal data to map the Cuprite district by the detection of silica content. Most satellite sensors, such as the Landsat 7 Enhanced Thematic Mapper Plus (ETM+), do not have the needed spectral resolution to identify specific mineral spectral features (Sabins, 1999). However, numerous studies have been done with multispectral remote sensing for the purposes of broad hydrothermal mineralization detection. Ruiz-Armenta and Prol-Ledesma (1998) studied the TM spectral response of hydrothermal alteration minerals in an area of the Transmexican Volcanic Belt. The two best techniques for enhancing the detection of alteration were found to be (1) principal components analysis, that is a statistical analysis to decorrelate the satellite image bands, and (2) HSI (hue, saturation, intensity) transformation, that is a simple non-linear transformation that can achieve a stronger color sense of an image without the larger statistical process of decorrelation (Ruiz-Armenta and Prol-Ledesma, 1998).

2.1. Instrument descriptions

2.1.1. AVIRIS

The AVIRIS instrument is a hyperspectral airborne instrument flown in a NASA high-altitude aircraft (Vane et al., 1987; Green et al., 1998; Rowan et al., 2000). It is commonly used for quantitative mineral mapping, vegetation surveys and as a calibration for spaceborne VNIR instruments (Hook and Rast, 1990; Clark et al., 1991; Kruse, 1999). Radiance data are recorded in 224 contiguous bands from the visible blue to the short-wave infrared region (0.4–2.5 μm), in 10-km swath widths that are commonly tens of kilometers long (Sabins, 1999). The spectral sampling interval is ≤10 nm (Macenka and Chrisp, 1987). The ER-2 aircraft collects data at the 20 m per pixel spatial resolution (high altitude) for all wavelengths. The Twin Otter aircraft collects data at a 4 m per pixel spatial resolution (low altitude).

The AVIRIS instrument itself consists of six optical subsystems and five electrical subsystems (Porter and Enmark, 1987). The optics subsystem consists of a whiskbroom scanner connected by optical fibers to four spectrometers. An onboard reference source is connected by optical fibers to the spectrometers, providing information on spectral and radiometric calibration (Macenka and Chrisp, 1987). In the spectrometers, the dispersed spectrum is imaged on cooled linear arrays of silicon detectors for the VNIR spectral range, and on iridium antimonide arrays for the NIR spectral range (Macenka and Chrisp, 1987). AVIRIS data are processed by the AVIRIS Data Facility at the Jet Propulsion Laboratory (JPL).

2.1.2. ASTER

The ASTER sensor is an imaging instrument currently flying on the Terra satellite (Yamaguchi et al., 1998; Pieri and Abrams, 2004). It was launched in December 1999 as part of NASA's Earth Observing System (EOS). ASTER contains three separate instrument subsystems (VNIR, SWIR, and TIR) with 14 bands from the visible green to the thermal infrared (0.52–11.65 μm). The instrument has a swath width of 60 km and a spatial resolution of 15, 30 and 90 m/pixel, in the VNIR, SWIR and TIR regions, respectively (Kahle et al., 1991). The VNIR subsystem has both a nadir-looking and backward-looking telescope used for the generation of optically derived digital elevation models (DEMs). The SWIR subsystem uses a single fixed refracting telescope; a platinum silicide-silicon detector is used in each SWIR channel. The TIR subsystem uses a Newtonian system with a primary mirror and lens. The telescope of the TIR subsystem is fixed and the mirror executes the pointing and scanning. Ten Mercury–Cadmium–Telluride detectors are in each TIR channel. A high-emissivity reference plate is used as an on-board calibration reference for the TIR subsystem.

2.1.3. THEMIS

Exploration of the Martian surface using remote sensing has been ongoing for nearly four decades. TIR remote sensing is one of the fundamental datasets used to assess the surface temperature, mineralogy,

surface rock abundance, and atmospheric composition on Mars (Christensen et al., 2000a). Current TIR instruments such as the Thermal Emission Spectrometer (TES) are continuing this legacy with increasingly higher spatial and spectral resolutions (Christensen et al., 2000b). However, with the recent emphasis on water and the search for potential life indicators on Mars, remote sensing has shifted to higher spatial resolution data in order to map these potentially small deposits (Farmer et al., 2001). The new THEMIS (Thermal Emission Imaging System) instrument has 10 multispectral thermal bands (100 m/pixel spatial resolution) in the 6.5–14.5 μm region as well as five bands (20 m/pixel spatial resolution) in the VNIR (Christensen et al., 1999). The increased spatial resolution may allow for more detailed mineral mapping on Mars, compared with the current 3 km/pixel resolution of TES. The primary goal of the THEMIS instrument, onboard the Mars Odyssey satellite, is to identify areas of past hydrothermal activity and determine the associated mineralogy. A secondary goal is to search for thermal anomalies associated with still-active hot springs on Mars (Christensen et al., 1999). Potential hydrothermal sites identified by THEMIS would likely become candidates for future landing sites and sample return missions.

Because detection of potential Mars relict hot springs will be done remotely, it is important to understand how to detect and study these deposits on Earth. The THEMIS spatial and spectral resolutions are comparable to ASTER. This similarity therefore allows ASTER data to be used as a terrestrial proxy for studies of geologic processes that have operated or are now operating on the Martian surface. Because the commonly required field-based validation necessary to verify model and mapping results is not possible at Mars, it is useful to take advantage of terrestrial analog site studies such as the hydrothermal features of Yellowstone Caldera.

2.2. Mineral detection using remote sensing

Thermal springs and their associated deposits have distinctive geometries and chemical signatures detectable by remote sensing (Walter and DesMarais, 1993; Ruiz-Armenta and Prol-Ledesma, 1998). Mössbauer spectroscopy was used to successfully identify hydrothermal alteration minerals near the vent, on the surface, and in the subsurface of iron-rich springs at Yellowstone (Wade et al., 1999).

Weathered or altered iron oxides are detected in the visible to near-infrared region (VNIR) with silicon sensing technology (Huntington, 1996). In the VNIR, materials containing Fe^{2+}, Fe^{3+}, Mn, Cr, and Ni produce different and identifiable spectra. There are variations in iron oxide species; for example, hematite is more abundant in stable landscapes, whereas goethite is more common in active erosional or depositional environments (Huntington, 1996). Goethite is a secondary iron mineral and forms in all types of hydrothermal replacement deposits (Chesterman, 1979). Aluminum substitution in iron oxides causes a wavelength variation of the 850–900 nm iron oxide crystal field absorption (Huntington, 1996). The VNIR is also the region for chlorophyll absorption (Huntington, 1996).

The SWIR is the overall best region for sensing the products of hydrothermal alteration, but not ideal for the detection of silica-rich minerals. Many clay minerals are bleached and hard to identify by the eye having non-distinct spectral features in the visible wavelengths. However' distinct absorption features are present in the SWIR, making it the best wavelength region to explore for hydroxyl bearing clays, sulfates and carbonate minerals that occur in and typify hydrothermal alteration systems (Huntington, 1996). The primary objective in this wavelength region is to map the spatial distribution and zones of hydrothermal alteration minerals containing OH^- groups. Phyllosilicates, Al(OH)-and Mg(OH)-bearing minerals, OH-bearing sulfates, ammonium bearing minerals, and carbonates can be mapped with SWIR. Pixels that have mixed spectral signatures can be separated, and semi-quantitative mineral abundance maps can be produced free of the diluting effects of vegetation; separation is possible in areas of up to 50% vegetation (Huntington, 1996). Detection of small proportions of some minerals is possible; targets such as veins that are smaller than a pixel may be mapped if they contain spectrally contrasting materials. It is also possible to map chemical substitutions, involving Na, K, Al, Mg, and Fe in SWIR spectra of micas, biotites, alunites, carbonates, and chlorites, as changes in cation composition give rise to measurable wavelength shifts (Huntington, 1996). For example, K-rich mica (muscovite) has a measurable absorption band at 2.207 μm.

However, a cation change from potassium to sodium gives rise to Na-rich mica (paragonite). Paragonite has a shifted absorption band at 2.189 μm.

SWIR (2–2.5 μm) remote sensing can be used to identify hydrothermal alteration deposits such as clay mineralogy (Hook and Rast, 1990; Clark et al., 1991). Clark (1993), Kokaly et al. (1998), and Kruse (1999) performed studies of Yellowstone's thermal areas using AVIRIS (4-m resolution) for mineral mapping. Kokaly et al. (1998) created mineral maps from AVIRIS data (20-m resolution). These maps showed the difference between the cooler, alkaline geyser basins and the hotter, acidic geyser basins, as a change in detected minerals from siliceous sinter and montmorillonite to alunite and kaolinite.

ASTER's 90-m TIR spatial resolution provides regional coverage useful for the overall characteristics of these hydrothermal systems, because it is capable of detection of hydrothermal silica (Sabins, 1999) and other rock-forming minerals. For example, Ramsey et al. (1999) discriminated mineralogical variations, including quartz content, within the Kelso sand dunes using airborne TIMS (Thermal Infrared Multispectral Spectrometer) imagery.

Huntington (1996) proposed a plan for detection of terrestrial and other potential planetary hydrothermal minerals. This includes field based mapping for ground-truthing purposes using field spectrometers, airborne mapping for detailed studies, and satellite mapping for regional scale characteristics. The proposal included an orbiting hyperspectral imaging system that can identify hydrous alteration minerals in places where the Martian surface has been disrupted by erosion or volcanic activity. An unmanned Fourier-transform VNIR spectrometer rover (400–2500 nm) was also proposed to detect the spectral signatures of these minerals. The basic outline followed in this study of Yellowstone incorporates Huntington's plan, using a combination of ground-truthing studies, airborne studies, and satellite studies.

3. Geology of the Yellowstone volcanic region

3.1. General background

The present geothermal activity of Yellowstone is a result of large-scale explosive volcanism that began 2 Ma ago and continued until about 70 ka ago (Christiansen, 1984; Walter and DesMarais, 1993). The Yellowstone plateau is composed of rhyolites, rhyolitic welded tufts and basalts (Christiansen, 1984; Walter and DesMarais, 1993). The distribution of active and recently active hydrothermal features in Yellowstone is shown in Fig. 1. Most of the hydrothermal features are located in the 0.6 Ma caldera, near the outer edge of the main ring fracture zone, or at the margins of the two resurgent domes (Fournier, 1989). Springs are scattered over several 1000 km^2 and there are approximately 3000 springs in about 100 clusters (Walter and DesMarais, 1993). Many clusters are grouped into geyser basins, which are areas of intensive geothermal activity (Walter and DesMarais, 1993).

Three major caldera eruptions occurred in the Greater Yellowstone ecosystem. The first and largest of these was 2 Ma ago and created the Island Park Caldera (volume >2450 km^3) (Embree and Hoggan, 1999). This eruption produced more than 2500 times the volume of volcanic material as the 1980 eruption of Mt. St. Helens Volcano (Christiansen, 1982; Embree and Hoggan, 1999). The remaining trace of this caldera rim, known as the Big Bend ridge, lies beyond the southern park border and extends west into Island Park, Idaho (Fritz, 1985; Embree and Hoggan, 1999). The welded Huckleberry Ridge Tuff produced from this cycle covers much of the Yellowstone region, lying on and beneath older rhyolite and basalt lava flows (Fritz, 1985; Embree and Hoggan, 1999).

Approximately 1.3 Ma ago, the second large eruption produced Henry's Fork Caldera, a smaller caldera centering around the Island Park, Idaho region (Christiansen, 1984; Embree and Hoggan, 1999). This eruption produced the Mesa Falls Tuff, an ignimbrite sheet that covered a volume of >2700 km^3 (Christiansen, 1982; Embree and Hoggan, 1999). This unit consists primarily of pyroclastic flows and lies outside of the park in Idaho, no exposures are found along the main roads in the park (Fritz, 1985).

The third and last caldera-forming eruption (0.6 Ma ago) created the present-day Yellowstone caldera (75 × 45 km) and Lava Creek Tuff of central Yellowstone National Park (Christiansen, 1984). Although some of the caldera rim has been covered by subsequent lava flows, much of the rim remains as a series of low hills along the central plateau. This last major

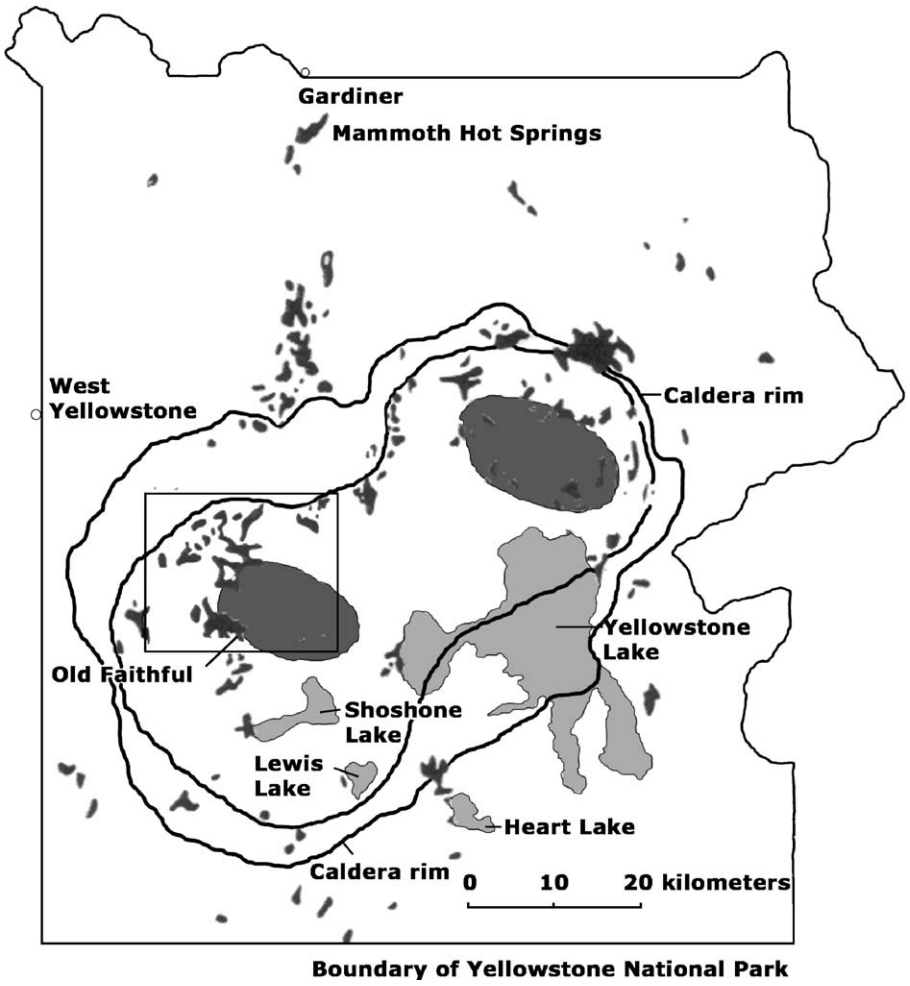

Fig. 1. Yellowstone National Park location map showing distribution of active and fossil hydrothermal systems (modified from Walter and DesMarais, 1993). Active and fossil springs are outlined in black. The Yellowstone caldera rim, two resurgent domes (dark gray), and lakes (light gray) are also shown. Black box shows the approximate location of study area.

series of eruptions produced about 1000 km^3 of welded-ash and basalt flows covering much of the park (Christiansen, 1982; Fritz, 1985; Embree and Hoggan, 1999).

Eruptions of varying size occurred after the last caldera-forming eruption (600–70 ka ago). The "West Thumb" of Yellowstone Lake is a secondary caldera produced by a smaller eruption approximately 150 ka old (Fritz, 1985). The Pitchstone Plateau was formed by rhyolite flows between 80 and 70 ka, and marks the last time lava flows erupted in the caldera (Harris and Tuttle, 1975; Fritz, 1985).

3.2. Lower Geyser Basin (LGB)

LGB is the largest thermal area in Yellowstone (19.3 km^2). It is geomorphically expressed as a flat plain covered with glacial sediments, large areas of siliceous sinter, and interspersed by lodgepole pine (Fig. 2). Rhyolite ridges surround the plain, forming steep escarpments in some sections. Glacial moraines border the ridges on the north and east sides, and extend into the basin. Geological evidence suggests that these moraines are the sites of pre-glacial hot springs (Marler, 1964). Groups of hot springs are

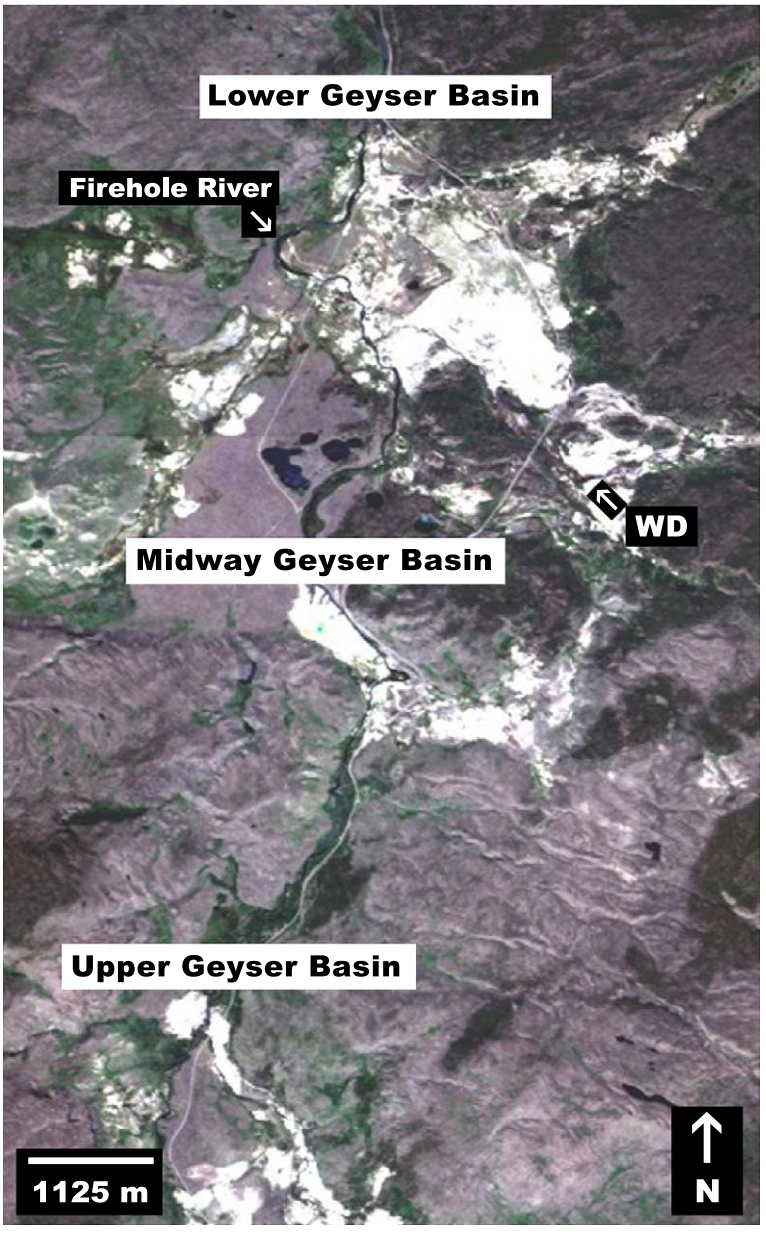

Fig. 2. AVIRIS visible reflectance color composite of the Lower, Midway, and Upper Geyser Basins of Yellowstone National Park with band 31 (0.666 μm) in red, band 20 (0.557 μm) in green, and band 12 (0.478 μm) in blue. Pixel resolution is 20 m. Geyser basins are defined in white and show broad regions of siliceous sinter.

widely scattered over the entire basin, but most are found in the eastern portion of the LGB. Even though the Lower Geyser Basin has a smaller number of geysers than other geyser basins, it is much larger in terms of hot water discharge volume (Marler, 1964).

3.3. Midway Geyser Basin (MGB)

The MGB is located in a low, flat-lying area (Fig. 2) that is topographically part of the Lower Geyser Basin, but separated by dense forests to the North

and West (Bryan, 1995; Smith and Siegel, 2000). East of this basin, Mallard Lake Dome was uplifted, creating two faults that run from southeast to northwest on the dome summit. The faults fracture the rock allowing rain and snowmelt to percolate downward and become heated. The brine then rises upward along fault fractures that supply hot water to Midway's hydrothermal features (Smith and Siegel, 2000). The hot springs extend along Firehole River for about 1.5 km, and then an additional 1.5 km along the Rabbit Creek drainage. Springs are numerous along both drainages, but geysers are scarce. Notable springs include Grand Prismatic Spring, the largest and deepest spring in Yellowstone (113 m in diameter and 34 m deep), as well as the powerful Excelsior Geyser and its tremendous discharge of water (Marler, 1964).

3.4. Upper Geyser Basin (UGB)

The UGB has an area of only 3.2 km^2, yet contains nearly one-quarter of all the geysers in the world (Fig. 2). It is part of the Firehole River Valley and is surrounded by cliffs on the west, northwest and east. The valley is drained by Firehole and Little Firehole Rivers, as well as Iron Spring Creek. Important geysers are located near the main rivers (Marler, 1964).

Small outcrops of the West Yellowstone rhyolite unit are located between Firehole River and Iron Spring Creek, but are mainly covered by glacial gravels and soil. In the southern section, glacial outwash, consisting largely of obsidian sand, covers the floor, but most of the basin is covered with siliceous sinter deposits from the hot springs (Marler, 1964).

4. Methodology

4.1. Field site selection

Field work was conducted in Yellowstone National Park from July 21 to August 2, 2001. Springs were surveyed over a large area, and included several in each geyser basin. Specific springs that exhibited variations in temporal activity, scale, types of deposits as well as near- to fully extinct springs, were also mapped. These areas were selected in consultation with National Park Service personnel to target areas of primary geologic interest for this specific study. The primary factors preventing full access to every site included safety and its popularity for tourism. Certain sites could not be sampled because they are located on thermal ground deemed too unstable. In most cases, popular sites were also ruled out, because the permit office restricts private research near tourists. Based on these criteria and restrictions, fourteen sites were ultimately surveyed (Table 1). Six active sites (Fig. 3A), five extinct sites (Fig. 3B), two near-extinct sites, and one active and extinct site were selected. Active sites are defined as sites that have geyser activity and surficial water runoff, and/or hot springs with an abundant water supply, generally in close association with colored bacterial mats. Near-extinct sites are sites of low discharge, having little water, no active geysers, and perhaps a few small hot springs. However, the term "near-extinct" should not be interpreted to mean that high flow rates will never resume at these sites. Changes to the subsurface connectivity of water pathways can take place over time with seismic activity, for example. Extinct sites are defined as sites with no geyser activity, dried-up hot springs, and/or lack of water in the area. Within these extinct sites, there is evidence of past geyser activity, indicated by a cone remnant and/or old sinter deposits. Finally, the active and extinct site was a large field site that had activity in one area and was extinct in another, with dense vegetation separated the active from the extinct site.

4.2. Site surveys

Each field site was analyzed using similar non-invasive methods. These included land cover analysis, photographs, GPS data collection, radiometric (temperature) analyses, and field spectroscopy. Field spectra were acquired using an Analytical Spectral Devices (ASD) FieldSpec Pro that collects information from visible to near infrared wavelengths (350–1100 nm). These data were acquired in order to map the small-scale spectral variations produced by the mineralogy, as well as for comparison to the AVIRIS and ASTER VNIR data. GPS data were collected with a Trimble Pro XRS dGPS receiver using a TSC1 assay surveyor data logger for sub-meter accuracy. The

Table 1
Description of field sites

Site No.	Name	Upper Geyser Basin	Midway Geyser Basin	Lower Geyser Basin	Latitude (N) UTM (meters) DMS	Longitude (W) UTM (meters) DMS	Activity	Notes
1	White Creek Group			•	4,931,116.56 44°31′ 59.51″	516,121.02 − 110°47′ 49.56″	Active	Small pools/ geysers; some extinct sinter deposits nearby
2	Firehole Lake Group			•	4,932,320.30 44°32′ 38.41″	517,459.31 − 110°46′ 48.7″	Near extinct/ extinct	Small pools filled with algae, fumaroles; areas of extinct sinter
3	The Ruin	•			4,922,805.00 44°27′ 30.34″	513,302.04 − 110°49′ 58.05″	Extinct spring	Near Myriad Group − highly active/ dangerous
4	Fortress Geyser			•	4,933,686.22 44°33′ 22.99″	513,325.51 − 110°49′ 55.98″	Active geyser	Large geyser with many sinter deposits
5	Rabbit Creek Hot Springs		•		4,929,557.73 44°31′ 9.06″	515,110.19 − 110°48′ 35.52″	Active geyser	Small geyser/ fumaroles surrounded by large extinct sinter field; surrounded by deep forest
6	Morning Mist			•	4,935,403.33 44°34′ 16.79″	515,239.04 − 110°48′ 34.40″	Near extinct	Many small pools and extinct large sinter areas
7	Fountain Flats			•	4,934,860.13 44°33′ 59.24″	514,463.98 − 110°49′ 4.26″	Extinct/ Near extinct	Extinct sinter areas and tiny nearly dried up pools/ mudpots surrounded by much vegetation
8	Extinct unnamed			•	4,932,182.75 44°32′ 34.02″	516,606.56 − 110°47′ 27.43″	Extinct	Dry cracked sinter surrounded by vegetation
9	Sunset Lake	•			4,923,289.66 44°27′ 46.16″	511,547.74 − 110°51′ 17.40″	Active	Large geothermal pool surrounded by extinct deposits
10	Sapphire Pool	•			4,925,719.40 44°29′ 4.91″	511,477.94 − 110°51′ 20.37″	Active	Large geothermal pool surrounded by extinct deposits
11	Mallard Lake Group	•			4,923,097.83 44°27′ 39.78″	514,063.34 − 110°49′ 23.58″	Active/ Extinct	Small active springs interspersed with extinct deposits; Heavily vegetated; scattered mudpots
12	Iris Group		•		4,929,700.49 44°31′ 13.81″	513,456.55 − 110°49′ 50.42″	Mostly extinct	Large extinct field with two moderately sized pools/active geyser nearby
13	White Dome			•	4,931,803.73 44°32′ 21.81″	515,660.31 − 110°48′ 10.36″	Active	Large highly developed sinter cone
14	Fracture Group	•			4,923,646.53 44°27′ 57.70″	511,985.32 − 110°50′ 57.57″	Extinct spring/ fumaroles	Small steam vents surrounded by extinct deposits

purpose of the GPS unit was to obtain the map coordinates of the main roads and tourist boardwalks in the park and to mark specific locations of spectral and temperature points at each site (Fig. 3). Non-real time differential corrections were done using base station points at Idaho Falls, Idaho.

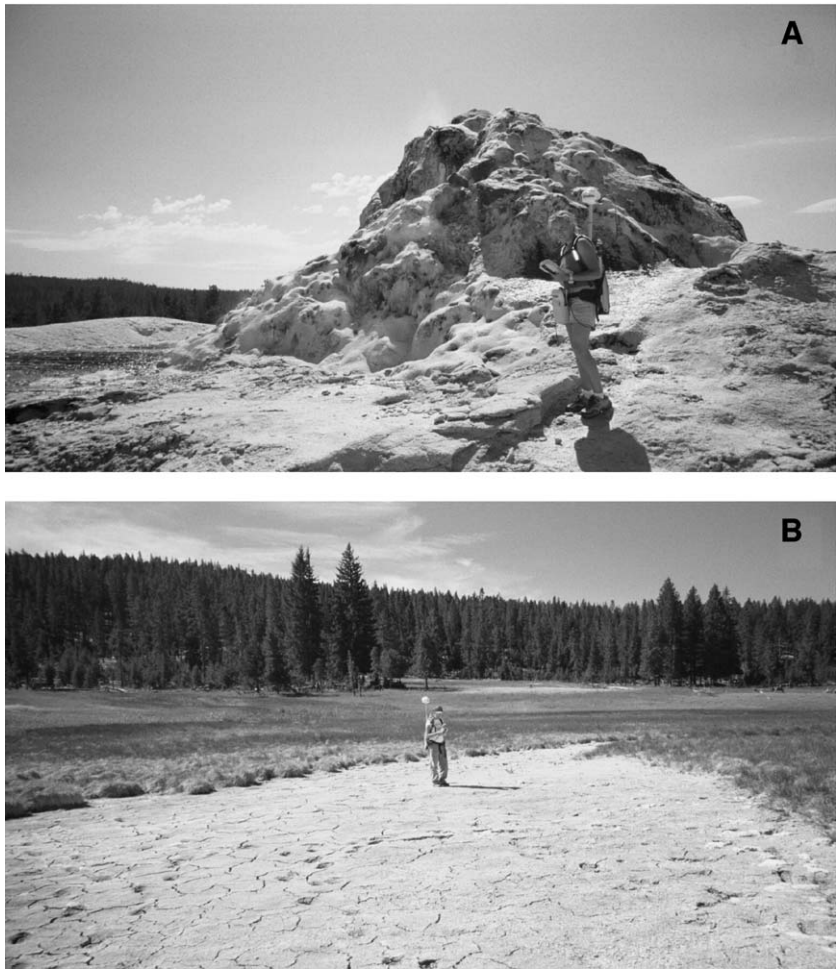

Fig. 3. Ground-level field photographs and GPS measurements at the Lower Geyser Basin (LGB) field sites. (A) The active White Dome Geyser (site 13), which is a prominent cone geyser exhibiting a wide range of sinter types, colors, and textures. (B) Survey at unnamed extinct field (site 8), which measures 29.6 × 10.6 m. The sinter is fractured in many places and the flat field is practically devoid of vegetation, although the surrounding region is abundant with green and dry grass.

4.3. ASTER data acquisition and processing

Two daytime ASTER level 1B (L1B) scenes were acquired on November 4, 2000, covering three geyser basins of Yellowstone National Park. The ASTER L1B dataset is the radiance at sensor, a calibrated and geometrically co-registered product. Further radiometric correction removes the sensor system detector error and the atmospheric influence on the radiance flux the sensor detects. The output of a radiometrically corrected image is the absolute radiance. Geometric rectification corrects the geometric distortion generated during image rendering. These scenes were initially georectified from metadata information, in order to obtain approximate latitude and longitude coordinates. Data validation studies involving GPS were conducted in the field in order to properly georectify the remote sensing images. The GPS data showed that the initial georectification was displaced by approximately 45–60 m for the VNIR and SWIR regions. Because the latitude–longitude coordinates were displaced, the second stage involved re-registration of the ASTER data using the GPS vector data, which resulted in <1 m error between the two data sets.

The absolute geometric accuracy of ASTER TIR is 90 m (one pixel), but initial georectification was deemed sufficient as the GPS overlay was not displaced. The ASTER level 2 (L2) products for VNIR and SWIR (radiance at ground and surface reflectance), and the TIR L2 products (radiance at ground, kinetic temperature, and emissivity) were obtained for the same scenes. The L1B and L2 data were ordered from a public domain through the Earth Observing System Data Gateway Distributed Active Archive Center (EDG DAAC). The higher L2 products were under a provisional release status and had not been fully validated by the ASTER science team at the time of the analyses. However, extensive work by Thome et al. (1998) and Ramsey and Dehn (2004) show that the data are well calibrated and the L2 processing algorithms appear to be working correctly.

4.4. AVIRIS data acquisition and processing

Airborne AVIRIS data are flown based on user requests and the availability of funding. The data for this work were previously collected and acquired through the AVIRIS project office at the Jet Propulsion Laboratory (JPL) under their graduate student use policy. These data are for the Lower, Midway, and Upper Geyser Basins of Yellowstone National Park. Three geometrically and radiance calibrated scenes were used from one flight line acquired on July 14, 1997 (Fig. 2). In order to convert AVIRIS data from radiance to reflectance, the data were corrected for the influence of several variables, including solar irradiance, atmospheric gas absorptions, and path radiance. These data were corrected using the Atmospheric Correction Now (ACORN) software program, which uses radiative transfer modeling (http://www.aigllc.com/acorn/intro.asp). Nash and Johnson (2002) determined that ACORN gave the closest match to laboratory spectra, in comparison to the Atmospheric Removal Program (ATREM) and the internal average reflectance (IAR) method.

Because AVIRIS is an airborne sensor, the same process used to georectify the ASTER images could not be used. The Environment for the Visualization of Images (ENVI) software supports image-to-map registration through Ground Control Points (GCPs). Image-to-map registration is a common technique that references an image to geographic coordinates from a vector overlay. GCPs were interactively defined and validated using the error terms displayed for specific warping algorithms. ENVI supports three different warping methods: Rotation/Scaling/Translation (RST), Polynomial, and Delaunay Triangulation. Three different resampling methods are supported: nearest neighbor, bilinear interpolation, and cubic convolution. An RST warp using nearest neighbor was performed because it produces the least amount of pixel to pixel averaging and yielded the best match to the actual vector data where compared to the other warping and resampling methods.

5. Results

5.1. Field-based VNIR reflectance spectra

During field surveys, the reflectance spectra of selected ground cover types were measured for active, near-extinct, and extinct springs. The type of spectra required was based on an on-site determination of the most common ground cover types at each field area. At each site, spectra for the various types of wet and/or dry sinter deposits and/or other mineral deposits, vegetation, and bacterial mats were collected. The total number of field spectra acquired and examined was 156, with each field representing a ground area of ~ 0.3 m. In this study, ''typical spectra'' refers to spectra collected at a single field site representing the characteristics of other field sites exhibiting similar thermal activity.

Typical field spectra for an active site (Site 1, White Creek Group) are shown in Fig. 4A. This particular unnamed group contains two pools and two smaller active microbial hot springs located near Octopus Spring. Hot springs bacterium and algae have unique spectra where compared with vegetation. Spectra 002 and 005 display the characteristic shape of Synechococcus, a common hot springs bacteria that creates a dark-green mat in the springs (Brock, 1994); the spectra are similar in shape to those of the bacteria identified by Kokaly et al. (1998). The chlorophyll absorption at 680 nm is narrow and the water absorption at 970 nm is strong. Red edge spectra at 765 nm and absorptions at 798 and 874 nm are seen. A minor absorption occurs at 620 nm that may reflect organics from the hyperthermophiles.

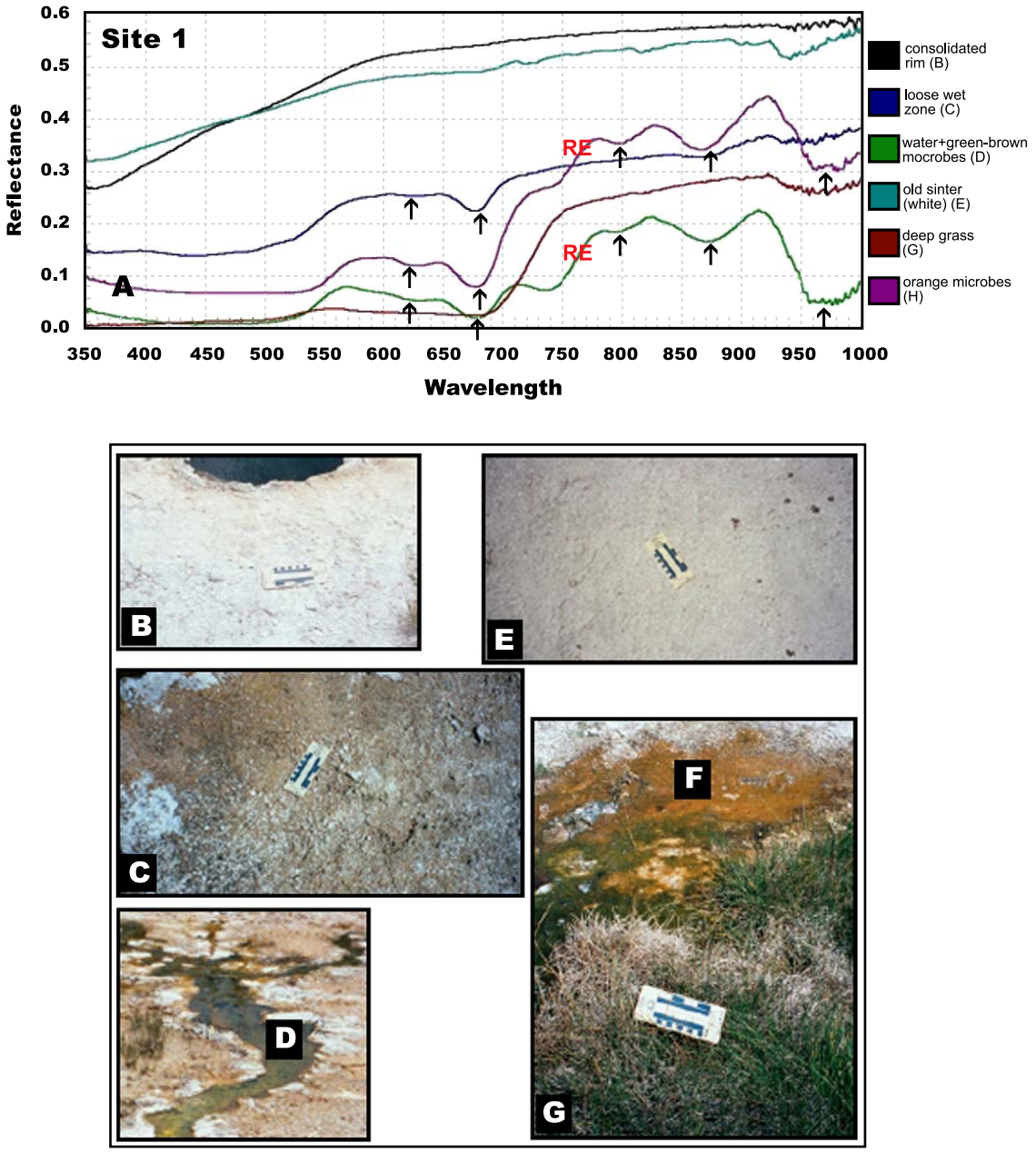

Fig. 4. Examples of the VNIR field spectra collected with the ASD instrument (wavelength range is 0.350–1.000 μm). (A) White Creek Group (site 1) is an active spring in the Lower Geyser Basin. Hot springs bacteria and algae have unique spectra compared to vegetation. Chlorophyll and water absorptions are also identified. Each photograph (B–G) shows the material for the particular field spectrum collected. (H) Iris Group (site 12) is an extinct spring in the Midway Geyser Basin. The extinct sinter has flat, featureless spectra in this region and vegetation spectra are also identified. Each photograph (I–M) shows the material for the particular field spectrum collected (see text for descriptions.)

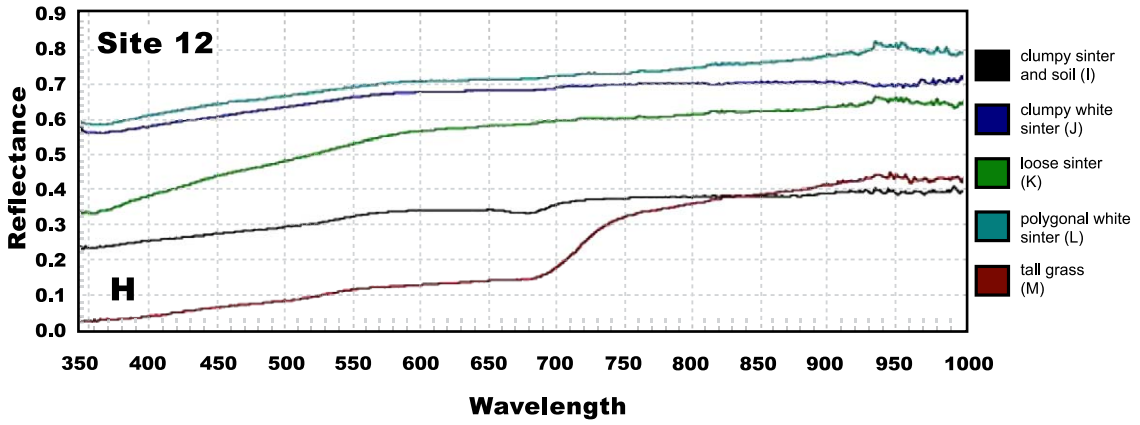

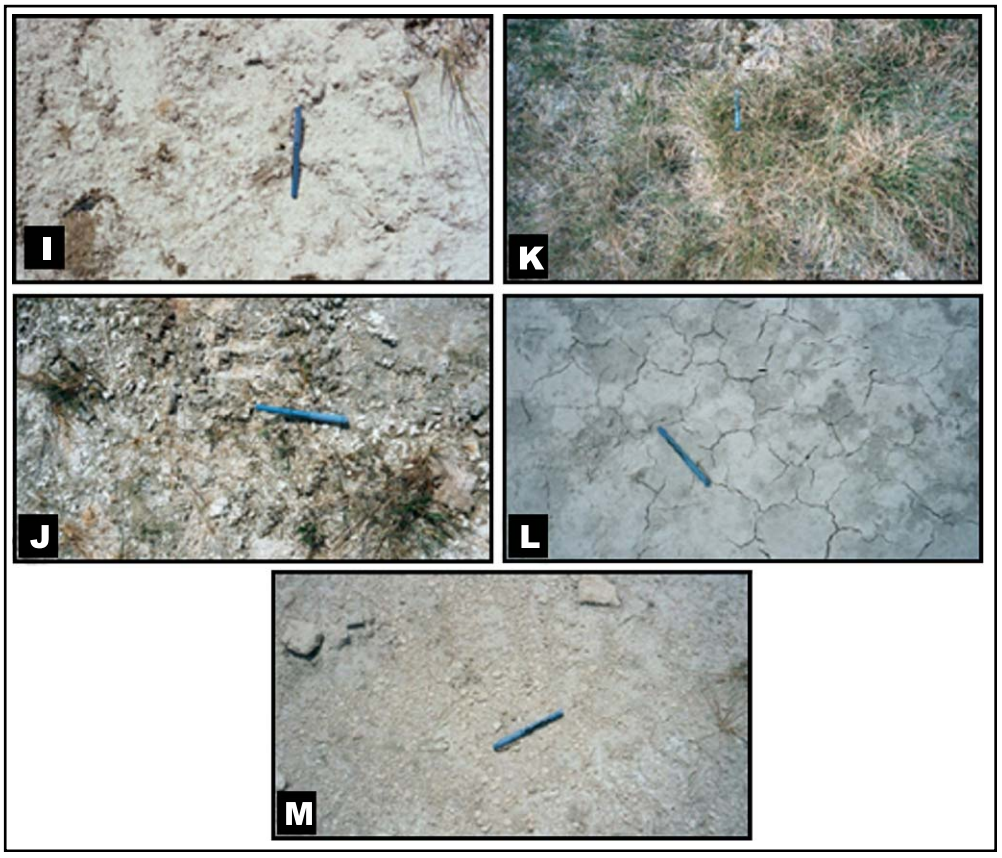

Fig. 4 (*continued*).

The strength of the water absorption is due to a thin layer of hot water running over the bacterial surface (Kokaly et al., 1998). In these active areas, the mineral signature is weak due to the overprinting of the water and bacterial cover (Kokaly et al., 1998). A slight iron oxide reflectance minima, caused by the charge transfer effect, was observed in some of the field spectra around 950 nm. A reflectance increase

was locally observed at around 550 nm, caused by iron oxide electronic transitions. Each field photograph in Fig. 4B–G shows the material for the particular field spectrum collected.

Typical spectra for an extinct site (Site 12, Iris Group) are shown in Fig. 4H. This site is a large extinct sinter field interspersed with some vegetation. Spectrum 00e is a vegetation spectrum, identified by its characteristic high reflectance due to chlorophyll in the near-infrared to red spectral region. The extinct sinter is siliceous (Spectra 00a–00d) and has a flat, featureless spectra in the VNIR. The active sites with visible microbes displayed a reflectance peak at about 560 nm. The prominence of this feature varied, but in most cases was evident. In the extinct sites, this peak was commonly subtle or absent. Bound water absorptions are absent. Each field photograph in Fig. 4I–M shows the material for the particular field spectrum collected.

5.2. ASTER VNIR reflectance spectra

The wavelength studied for the VNIR ranges from 0.55–0.82 μm. The field sites ranged in size from 1–10 pixels on the ASTER and AVIRIS images, where one pixel represents 15 and 20 m, respectively.

ASTER VNIR spectra of an active site (Site 9, Sunset Lake) and an extinct site (Site 7, Fountain Flats) are shown in Fig. 5A and B, respectively. Site 9 is part of the Biscuit Basin, which is surrounded by rhyolite cliffs. The cliffs are mostly grass and tree covered, most of which were burned from the large fires of 1988 (Franke, 2000). The site is a large geyserite field near Sunset Lake, bordered by a stream on one side. Sinter deposits are abundant, but darker sinter is less abundant. Site 7 has a small stream that bisects the area. There are also some mudpots and pools, but no active geysers. Vegetation covers most of the area, except over the extinct patches of sinter.

ASTER VNIR spectra for the active and extinct sites are dominated by vegetation. Band 3 is located in the near-infrared and shows a large reflectance increase (red-edge). Band 2 is located in the visible red and chlorophyll absorption dominates. Band 1 is located in the visible green; here, a chlorophyll reflectance peak is present in some of the spectra. All of the active sites, with one exception, exhibited the band 1 reflectance peak. More than half of the extinct sites lacked the band 1 peak. Other VNIR spectral differences between active sinter and extinct springs could not be distinguished. Probable reasons for this include the large pixel size (15 m) and the inability to accurately identify hydrothermal alteration in the VNIR wavelength region, especially in conjunction with the broad band passes of ASTER. The spectra indicate sub-pixel mixing, as they do not resemble dry or green grass. Reflectance in the visible red and green is higher for these spectra than grass spectra.

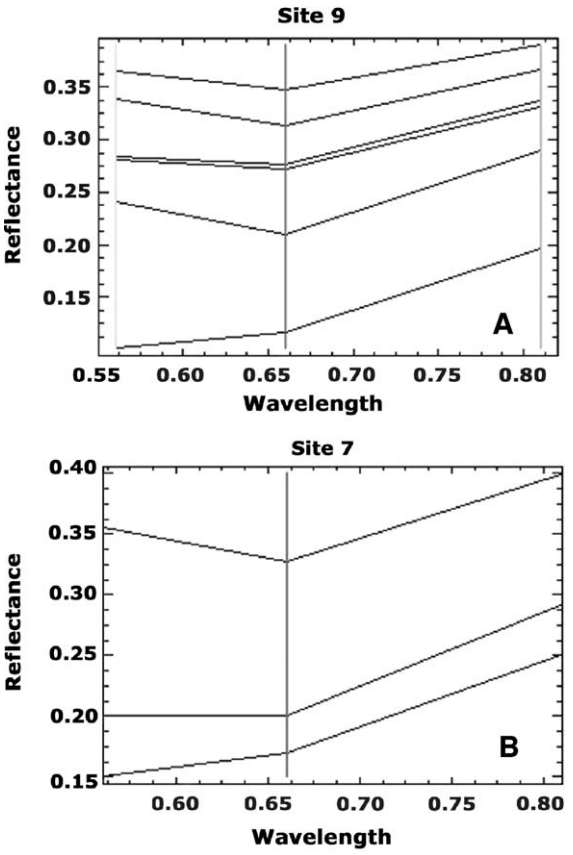

Fig. 5. ASTER VNIR reflectance spectra, with band 3=(0.76–0.86 μm), band 2=(0.63–0.69 μm), and band 1=(0.52–0.60 μm). (A) Sunset Lake (site 9) is an active spring in the Upper Geyser Basin. (B) Fountain Flats (site 7) is an extinct spring in the Lower Geyser Basin. The spectra are vegetation dominated, however they do not resemble pure vegetation. Spectral mixing with the soil background is likely because of the higher reflectance in the 0.52–0.69 μm region.

5.3. ASTER and AVIRIS SWIR reflectance

The SWIR wavelength examined spanned from 1.65–2.4 μm. The field sites ranged in size from 1 to 9 pixels on the ASTER and AVIRIS images, where one pixel represents 30 and 20 m, respectively.

AVIRIS SWIR spectra of an active site (Site 13, White Dome) are shown in Fig. 6A. White Dome (Fig. 3 left) is a prominent cone geyser with several runoff channels branching from the dome. A wide variety of different sinter types, colors, and textures indicate the dome underwent several changes over time. The older domes are visible and are located underneath the newer domes. Eruptions from this geyser are frequent, short and irregular. Black algae and brown bacteria are present in the runoff channels located on the eastern portion of the dome.

Kruse (1999) found that siliceous sinter has a characteristic spectrum in the AVIRIS SWIR region (Fig. 6B). In comparison to the AVIRIS spectra in this study (20 m pixels), Kruse's spectrum comes from smaller (4 m) and therefore presumably less mixed AVIRIS pixels. In Fig. 6B, the broad, shallow reflectance minimum gradually increases from 2 to 2.1 μm and decreases from 2.1 to about 2.25 μm. There is an absorption feature at ~2.25 μm, with reflectance generally increasing to 2.4 μm, where another subtle reflectance peak is observed. Finally, the reflectance decreases longward of 2.4 μm. Thus, a key reflectance peak is at 2.4 μm, and a key absorption is at 2.25 μm. The active site spectra in Fig. 6A are similar in shape to the silica sinter spectrum of Kruse (1999) although the 2.25-μm feature is not as deep, and reflectance decreases longward of this wavelength; hence there is no reflectance peak at 2.4 μm.

AVIRIS SWIR spectra of an extinct field (Site 12, Iris Group) are shown in Fig. 7A. This sinter field

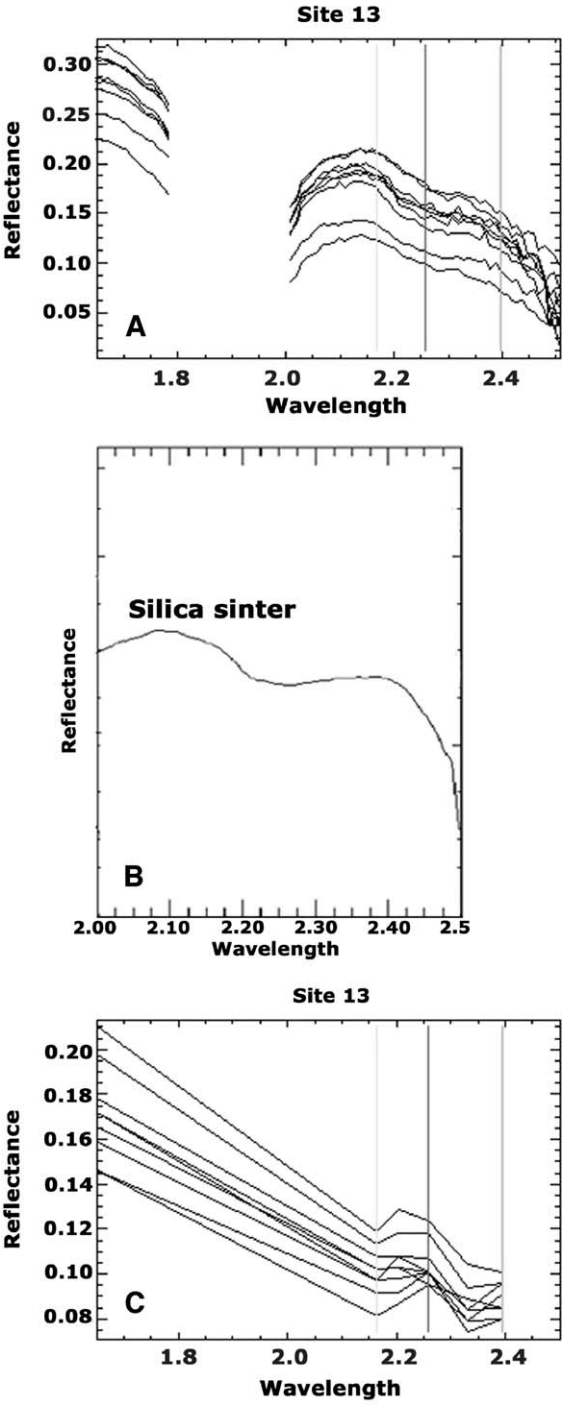

Fig. 6. SWIR reflectance spectra from White Dome (site 13) in the Lower Geyser Basin (an active spring). (A) AVIRIS spectra (1.65–2.51 μm) showing the absorption feature of siliceous sinter at 2.25 μm. (B) AVIRIS spectra of silica sinter as observed by Kruse (1999) (note, only relative reflectivity was displayed on the y-axis of the original figure). The spectrum is similar in shape to the spectra in (A), and especially similar to the spectra in Fig. 7A. (C) ASTER reflectance spectra (1.65–2.40 μm) showing that the siliceous sinter cannot be easily identified due to the broader spectral band passes. The spectra most resemble a mix of dry and green vegetation, but significant spectral mixing occurs.

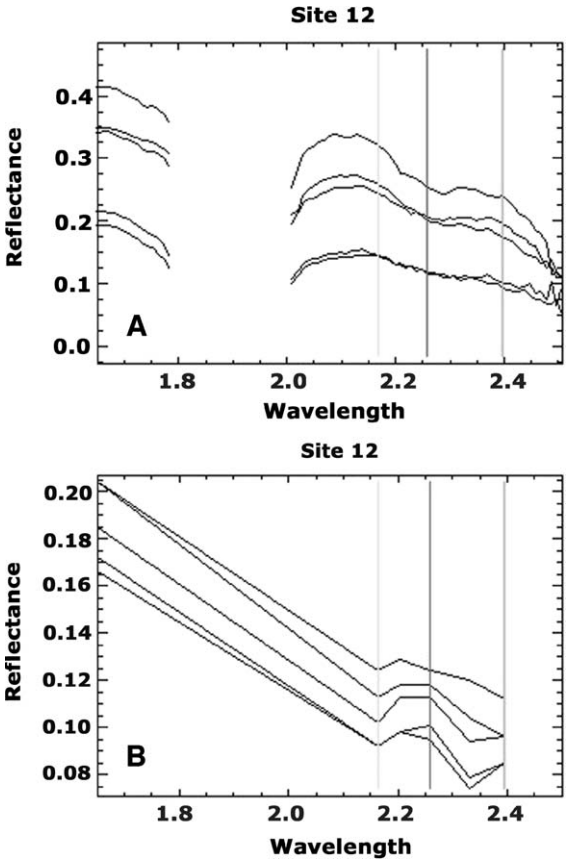

Fig. 7. SWIR reflectance spectra from the Iris Group (site 12) in the Midway Geyser Basin (an extinct spring). (A) AVIRIS spectra (1.65–2.51 μm) have a deeper absorption feature of siliceous sinter at 2.25 μm as compared to Fig. 6A. A subtle reflectance peak is also located near 2.4 μm and not observed in the active site spectra. (B) ASTER reflectance spectra (1.65–2.40 μm) also showing the lack of a positive identification of siliceous sinter. The spectra most resemble a mix of dry and green vegetation, but significant spectral mixing occurs.

occupies much of the basin; therefore it is easily detected in the ASTER (30 m pixel) and AVIRIS (20 m pixel) SWIR data. The spectral morphology of the sinter from the extinct site (Fig. 7A) closely resembles that of the silica sinter spectrum in Fig. 6B, observed by Kruse (1999). Fig. 7A also resembles the spectral morphology of the sinter from the active site (Fig. 6A), with some notable differences, including a deeper 2.5 μm absorption and the presence of a 2.4-μm peak.

Figs. 6A and 7A have subtle signatures because these are spectra of natural, rather than pure laboratory, materials. Key absorptions can be identified at the aforementioned locations through careful analysis of the overall shape of the spectra. Also, spectral signatures are subtle because the SWIR region is not sensitive to silica-rich minerals. Minerals like quartz and feldspars have no sharp absorption features and can only be detected by the presence of trace minerals and/or atoms. For example, Fe-rich silicates like olivine or' in this case, the water present in the sinter.

Absorption depths and reflectance peaks were precisely determined by (1) quantitatively measuring these features and (2) matching both *x*- and *y*-axes and overlaying of the spectra to compare the morphology of the active and extinct surfaces. For most of the extinct sites examined, the absorption depth of the 2.25-μm feature is deeper and more pronounced than the active spectra. The 2.25-μm absorption depth is proportional to the abundance of sinter on the surface. However, the entire spectrum indicates siliceous sinter, not just that one absorption feature at 2.25 μm. At 2.2 μm, there are minor absorptions, indicating the presence of small amounts of clay minerals, such as montmorillonite and kaolinite.

Near 2.4 μm, most of the extinct site spectra have a small reflectance peak that is not observed in the active site spectra. The 2.4-μm reflectance peak is absent from the active sites because the sinter is wet, and the water may be suppressing it (Kruse, 1999). Spectral mixing could also be responsible for lack of the 2.4-μm reflectance peak. However, for those extinct spectra that lacked the reflectance peak, reflectance does not decrease as greatly longward of 2.4 μm as it does in the active spectra, indicating that a trace of the reflectance peak remains.

The ASTER SWIR spectra of both the active and extinct sites are shown in Figs. 6C and 7B, respectively. The siliceous sinter absorption feature at 2.25 μm cannot be easily identified because of the broader spectral band passes. The spectra most resemble a mix of dry and green vegetation, with a small reflectance peak at 2.2 μm and absorption at around 2.37 μm, but more spectral mixing occurs in the ASTER 30 m pixels than in those of AVIRIS.

Overall, spectra for the Lower, Midway, and Upper Geyser Basins indicate broad regions of siliceous sinter combined with small amounts of clays (i.e. montmorillonite) and other minerals (i.e. iron oxide) in some areas. The dominance of the siliceous sinter

in these basins indicates the presence of neutral to alkaline waters. White et al. (1988) proposed that montmorillonite and siliceous-sinter are formed from neutral pH waters high in chlorine and quartz (Kokaly et al., 1998), such as those waters in the Lower, Midway, and Upper Geyser Basins. More acidic hydrothermal systems, such as Norris Geyser Basin, contain higher amounts of clays and sulfate minerals associated with more acidic waters (Clark, 1993).

5.4. ASTER and AVIRIS band ratios

Al–OH and Mg–OH rotational effects associated with clays and other hydroxylated minerals result in absorption in ASTER band 6 and AVIRIS band 195 (Sabins, 1999). Hydroxyl absorptions are caused by overtone and combination bands of primary OH^- molecular vibrations located at wavelengths longer than 2.5 μm (Vincent, 1997). Overtone bands occur at wavelengths where the frequency of a primary absorption band is doubled, tripled, etc., and combination bands occur where the frequencies of two primary bands are added (Vincent, 1997). The locations of the OH^- absorption bands depend on the position of the hydroxyl ion in the crystal lattice (Vincent, 1997).

The Landsat TM 5/7 band ratio highlights altered clay-rich rocks, with a high ratio indicating a high degree of hydrothermal or clay mineral alteration (Sultan et al., 1987). This ratio corresponds to the ASTER 4/6 band ratio and the AVIRIS 139/195 band ratio, or 1.67 μm/2.22 μm. Table 2 shows the ASTER and AVIRIS band ratios for the fourteen field sites. Altered rocks typically have ratios greater than unity (Sultan et al., 1987). All the field sites had 4/6 ratios and 139/195 ratios greater than unity, indicating that the band ratio technique accurately identified the rocks present at field sites as hydrothermally altered. Although in most cases, the ASTER and AVIRIS ratios were similar to one another, the AVIRIS ratio was slightly greater than that derived from ASTER data (Table 2). The higher AVIRIS ratio is probably a result of the narrower band passes of the hyperspectral data. Narrower AVIRIS band passes will yield different results then the ratios calculated from the multispectral ASTER data sets. The sites that exhibited the highest ratios were active Site 13 (ratio = 2.33) and extinct Site 12 (ratio = 2.16). Most of the extinct spring sites not masked by vegetation (i.e. Sites 7, 8 (Fig. 3B), and 12) had a higher 4/6 ratio than active spring sites. Sites 3, 6, and 14 are extinct sites with vegetation covering the alteration, and do not have high 4/6 ratios. The extremely active sites (i.e. Sites 9, 10, and 13; Fig. 3A) have high 4/6 ratios, but their ratios were not as high as the extinct sites. The only exception is Site 4, a very active site exhibiting a high 4/6 ratio (ratio = 1.95).

Table 2
ASTER 4/6 and AVIRIS 139/195 SWIR band ratios

Site No.	ASTER 4/6 ratio	AVIRIS 139/195 ratio
1 White Creek Group	1.53–1.55	1.55–1.61
2 Firehole Lake Group	1.34–1.42	1.37–1.46
3 The Ruin	1.63	1.41
4 Fortress Geyser	1.69–1.71	1.65–1.95
5 Rabbit Creek Hot Springs	1.54–1.61	1.21–1.25
6 Morning Mist	1.40–1.76	1.55–1.66
7 Fountain Flats	1.57–1.78	1.42–1.87
8 Extinct unnamed	1.61–1.66	1.78–1.93
9 Sunset Lake	1.48–1.65	1.43–1.54
10 Sapphire Pool	1.55–1.58	1.60–1.62
11 Mallard Lake Group	1.66–1.86	1.28–1.76
12 Iris Group	1.58–1.73	1.80–2.16
13 White Dome	1.59–1.68	1.00–2.33
14 Fracture Group	1.48–1.53	1.33–1.34

5.5. ASTER TIR emissivity and temperature

Hydrothermal silica occurs in the form of quartz and is an important component of most hydrothermal alteration systems. Because silica and other rock-forming minerals have unique spectral features in the TIR region, remote sensing instruments such as ASTER with multispectral TIR systems are ideal for detection of these minerals (Gillespie et al., 1984; Hook et al., 1994). Fig. 8 shows an ASTER TIR image (bands 14, 12, 10) of the Lower Geyser Basin. The entire basin is bright compared to the surrounding region, indicating a large thermal anomaly (~ 19.3 km^2). In most cases, the active and extinct hot spring areas within the basin are brighter (i.e. warmer) than the overall basin. No detail of the hot springs can be seen in this resolution; only a bright pixel(s) representing the thermal area is evident.

At the time of the analysis of this study, the ASTER L2 temperature/emissivity (TES) algorithm was not fully validated. Although the ASTER emis-

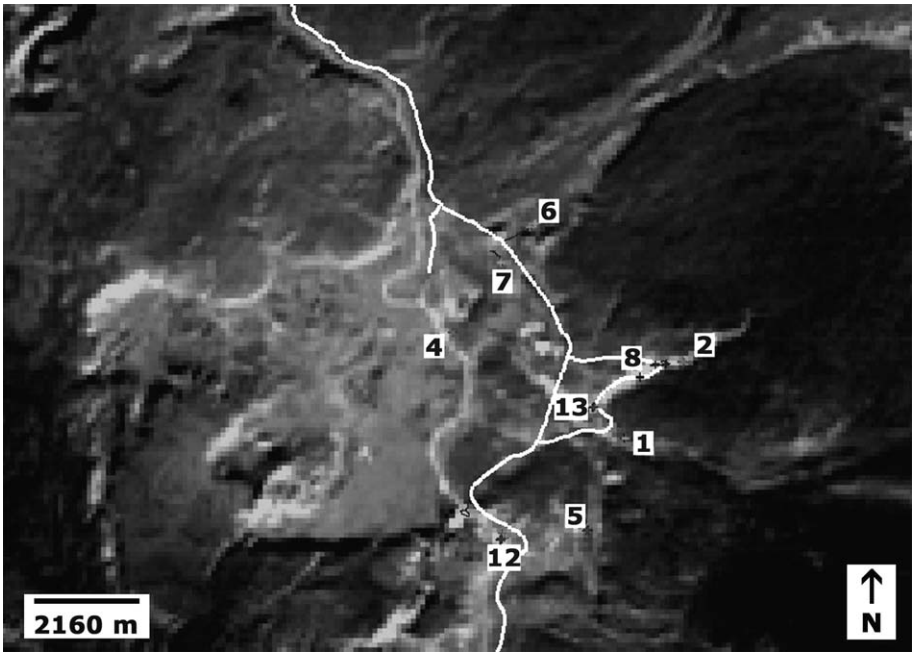

Fig. 8. ASTER TIR image of the Lower and Midway Geyser Basins with GPS overlay, with band 14 (10.95–11.65 μm), band 12 (8.925–9.275 μm), and band 10 (8.125–8.475 μm). Field sites within the basin are numbered. The entire basin is brighter than the surrounding region, indicating a large thermal anomaly. Active and extinct hot spring areas within the basin are brighter (warmer) than the overall basin, however, the individual hot springs cannot be identified at this resolution.

sivity and surface kinetic temperature products were examined, many of the field sites had emissivity values greater than 1.0. Because true emissivity values range from 0 to 1, the ASTER L2 emissivity product was deemed insufficient and not used. In its place, the emissivity normalization technique was implemented, with a maximum assumed emissivity of 0.985 (Realmuto, 1990).

The field sites occupied an area far less than one ASTER 90 m TIR pixel. Most of the field sites resembled the emissivity spectrum of silica, with a primary emissivity low at approximately 9.2-μm. The depth of the 9.2 μm feature is proportionally related to the abundance of silica (Hook et al., 1992). The emissivity value for the depth of the 9.2-μm absorption feature was averaged for the active and extinct sites. The active sites had an average emissivity depth of 0.9665, whereas the extinct sites had an average emissivity depth of 0.9622. Although the difference between the average emissivity depths of the active and extinct sites (0.43%) may not be significant, one must keep in mind that these values are averages. Many of the emissivity differences were far greater than 0.43%. More importantly, the extinct sites consistently had deeper emissivity absorption bands than the active sites, which is significant because the active and extinct sites are composed of essentially the same material (silica). Therefore, the extinct sites appear to contain more silica than the active sites. This may be the result of an actual abundance difference between the two types of surfaces, with silica being preferentially concentrated at the extinct sites as other more mobile minerals are removed by weathering. Alternatively, because finer-grain particles produce a lessening of TIR absorption features, the extinct sites either have less fine-grain particles or these mineral grains have been welded over time with weathering.

Rocks with increasingly mafic mineralogies exhibit bands that shift to longer wavelengths (Hunt, 1980; Kahle, 1987; Salisbury and D'Aria, 1992). The emissivity spectra showed no band shifts at any of the field sites, as all of the sites had a distinct absorption feature at 9.2 μm, indicating that the sites had the similar felsic silica mineralogies.

The ASTER acquisition date was November 2000, and although the geothermal features do not vary dramatically in temperature throughout the year, mixing of ground cover types (including mineral deposits, vegetation, rock/soil, and water) is assumed. Because of this mixing in the 90-m spatial resolution of the TIR, the derived kinetic temperatures were not as high as the temperatures measured with the field radiometer. Most of the active sites visited had small thermal features (from ~1 to 30 m^2). The largest active thermal feature was at Sunset Lake, corresponding to a third of a pixel in the ASTER TIR region. The extinct fields were generally larger in size (from ~30 to 270 m^2). The largest extinct thermal feature was at the Iris Group, corresponding to several pixels in the ASTER TIR region. The active sites with the highest kinetic temperatures were 9 and 13 (17.2 and 9.3 °C, respectively), whereas the highest temperatures for the extinct sites were 8 and 12 (15.9 and 11.9 °C, respectively). The other sites ranged in temperature from 2.9 to 7.1 °C. Because several of the extinct springs had high measured temperatures, high heat flow can be present at sites no longer considered active.

6. Application to Mars

There are several possible sites on Mars designated as areas of past (or present) hydrothermal activity (Bulmer and Gregg, 1998; Gulick, 1998; Nelson et al., 1998; Dohm et al., 2000). Indirect evidence of near-surface water includes the region surrounding Apollinaris Patera (90°S 186°W), an ancient Martian volcano, located in the Elysium Basin-Terra Cimmeria region (Farmer, 2000). The chaos features and outflow channels are abundant near the volcano base and could have formed by subsurface cryosphere melting (Farmer, 2000). The proximity of the chaotic features to the volcano suggests the possibility of prolonged hydrothermal activity (Farmer, 1996, 2000). Potential direct evidence of near-surface water has also been recently detected with the Gamma Ray Spectrometer also onboard the Mars Odyssey spacecraft (Boynton et al., 2002).

The Thermal Emission Spectrometer (TES) instrument onboard the Mars Global Surveyor (MGS) detected a large specular (coarse-grained) gray hematite deposit at Sinus Meridiani (Christensen et al., 2000b). Because this type of hematite is thought to have formed by aqueous precipitation at high temperatures, its discovery may be evidence that hydrothermal systems could have operated on Mars in the recent past (Christensen et al., 2000b; Farmer, 2000). Coarse-grained hematite is generally found in volcanic regions, such as the Yellowstone hydrothermal system, and forms as hot water percolates through iron-bearing rocks (Christensen et al., 2000b). As the water cools, the iron dissolves and precipitates in cracks and veins of the surrounding rock. The gray hematite can also form as large amounts of iron are dissolved in large bodies of water (Christensen et al., 2000b).

The THEMIS instrument is being used to detect mineralization and potential thermal anomalies associated with hydrothermal activity, although thus far none have been identified. Targeting these hydrothermal sites is seemingly possible, given the comparatively high (100 m/pixel) spatial resolution of the instrument. A number of hydrothermal minerals, including silica, carbonates, and hematite, if exposed at the surface in sufficient quantity and aerial abundance, should be easily identified (Thorsos et al., 2002). As mentioned earlier, ASTER and THEMIS are both multispectral, having similar spatial and spectral resolutions. In this study, ASTER was not very capable of identifying hydrothermal minerals using SWIR spectroscopy alone, although it identified areas of alteration using SWIR band ratios. Hyperspectral instruments such as AVIRIS are necessary for the detection of specific hydrothermal minerals if only SWIR spectroscopy is used. Therefore, the lack of a SWIR region on THEMIS is not a major issue because THEMIS is multispectral and SWIR is not the prime region for the identification of silica-rich minerals. ASTER proved successful in identifying thermal alteration anomalies in the TIR region. Thus, THEMIS should be able to identify hydrothermal areas in the TIR region if they still exist on Mars.

A THEMIS VNIR image of Terra Meridiani region is shown in Fig. 9. This area lies at eastern boundary of the hematite unit (1.471°N, 359.468°W). The variations of brightness and texture of the surface seen in this image can be attributed to different rock layers (Christensen, 2001; Lane et al., 2003). Numerous layers exposed across the surface may indicate

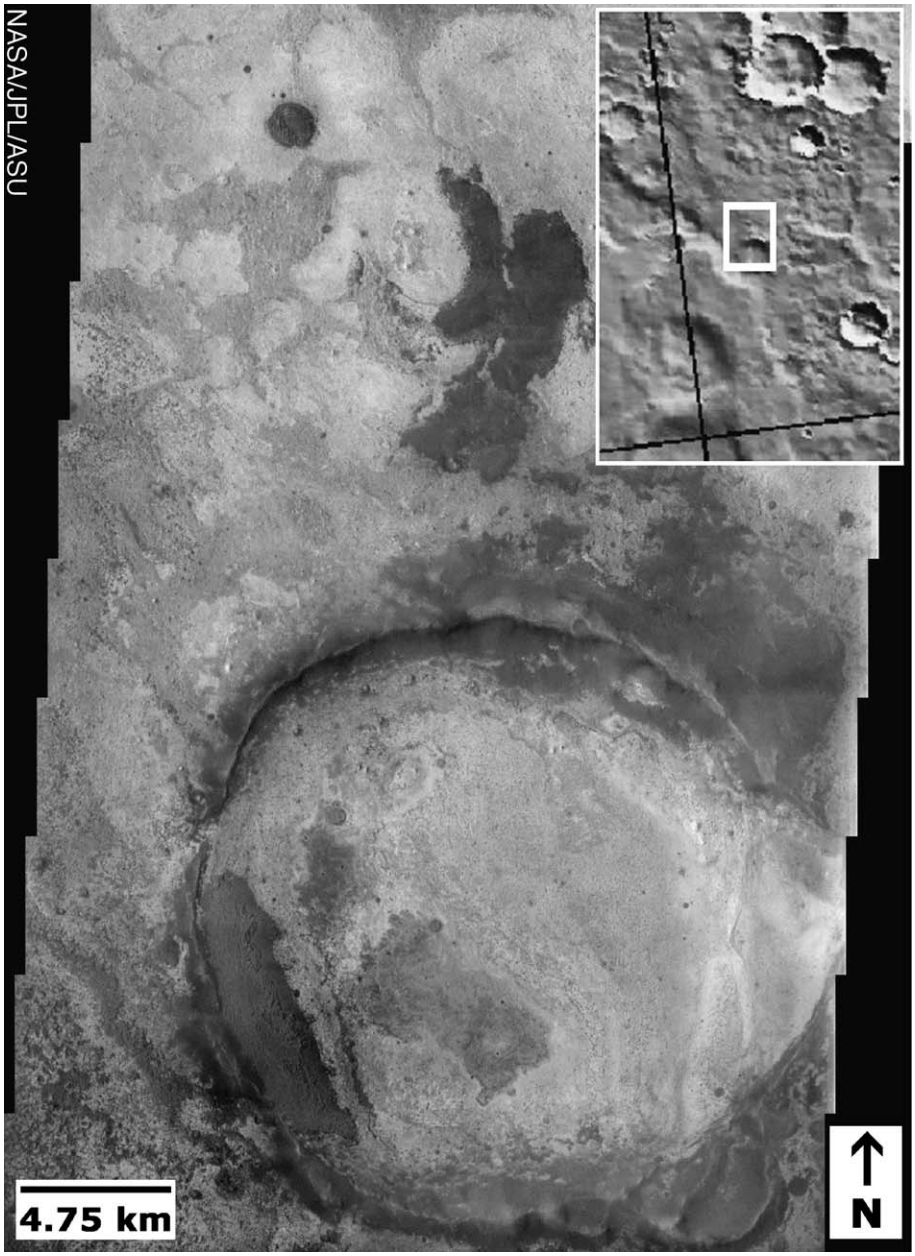

Fig. 9. THEMIS VNIR image of Terra Meridiani, Mars at location: 1.471 N, 359.468 W. Viking orbiter context image is shown. Variations of brightness and texture of the surface seen in this image can be attributed to rock layers with different thermophysical properties. Numerous layers exposed across the surface may indicate extensive volcanic and sedimentary deposition, followed by erosion. The 19-km diameter crater located in the southern portion of the image shows distinct layering, possibly sedimentary in origin (image courtesy of NASA/JPL/Arizona State University, http://themis.la.asu.edu).

extensive volcanic and sedimentary deposition, followed by erosion (Lane et al., 2003). The 19 km diameter crater, located in the southern portion of the image, shows distinct layering that is perhaps sedimentary in origin. Different temperatures within these rock layers are shown by THEMIS infrared images of this area, indicating varying physical properties in each layer (Lane et al., 2003). The temperature differences suggest temporal variations in environmental conditions as these layers were deposited or solidified. The hematite site has been designated as a landing site for the 2003 Mars Exploration Rover (MER) missions. MER will have two identical rovers going to two different sites.

The second landing site will be Gusev Crater (14.82°S, 184.85°W). These sites were selected because they may be modified by water at some time in their history. For the hematite site, the hydrothermal deposits are thought to be located in the ejecta blanket of a 19 km crater (near 2°S, 6°W) (Newsom et al., 2003).

At Yellowstone, siliceous sinter deposits are common constituents of the Lower, Midway, and Upper Geyser Basins. These deposits have been cited as important targets in the search for an ancient biosphere on Mars (Walter and DesMarais, 1993; Farmer, 2000). Guidry and Chafetz (1999) showed microbes are well-preserved in old siliceous sinter deposits in Yellowstone. By studying the reflectance and emissivity spectra of these deposits at the resolution of ASTER, the spectral signatures of these potential terrestrial analogs can be applied to TIR data of Mars in order to detect similar deposits. The ASTER TIR images of the Lower, Midway, and Upper Geyser basins were resolution degraded from 90 m/pixel to the THEMIS 100 m/pixel resolution. This 10 m change was not spatially significant, but shows that thermal anomalies of the larger individual active and extinct hot springs can still be accurately identified. The ASTER TIR images were also resolution degraded to the TES 3 km/pixel resolution. This change was spatially significant, and the thermal anomalies of the hot springs could not be accurately identified.

To this date, the only aqueous mineral identified on Mars is hematite. Poor spatial resolution may be a reason why hydrothermal deposits and other sedimentary or aqueous minerals, including carbonates and evaporites, have not yet been located. Another possibility is that the aqueous mineral deposits could be dust-covered and/or eroded, thereby suppressing or erasing their spectral signatures. Finally, it may be that there is a low abundance of aqueous minerals on Mars. None of these possibilities can be favored until more extensive research with newly developed instruments is completed.

Although the thermal areas of Yellowstone contain hematite, such as the Chocolate Pots region of the Gibbon Geyser Basin, hematite is not present in such mass quantities as the hematite region on Mars. In fact the Martian hematite region is larger than any terrestrial hematite deposit known to have originated through hydrothermal activity (Christensen et al., 2000b). This may indicate a significant difference regarding the formation and types of hydrothermal minerals found on Mars. Alternatively, the greater hematite abundance on Mars may be attributed to different scale factors than the Earth. In general, features on Mars are roughly ten times larger compared to Earth, due to lower gravity, crustal stability from lack of plate tectonics, and lower erosion rates than the Earth.

7. Conclusions

Active and extinct springs have differences detectable by remote sensing. Techniques that proved to be useful in this discrimination included field VNIR spectroscopy, AVIRIS SWIR reflectance, ASTER and AVIRIS band ratioing, and ASTER TIR imagery, including emissivity and temperature. Each selected study area had unique characteristics detectable by the field and remote sensing techniques employed in this study. For example, the active springs had strong water and chlorophyll absorptions that set them apart from the extinct springs. For the extinct spring sites, field VNIR spectroscopy showed featureless spectra, except in vegetated areas, where red edge spectra dominated. Most active springs exhibited bacterial signatures detectable by field VNIR spectroscopy. Field spectra detected unique spectral characteristics of the hyperthermophiles; this provides a basis for understanding how such organisms (most likely in fossil form) might be recognized on Mars.

Upon initial examination, the AVIRIS SWIR reflectance for both the active and extinct springs look similar. However, the extinct springs have a deeper

and more distinct 2.25 μm absorption feature than the active springs. Also, most of the extinct site spectra have a subtle reflectance peak near 2.4 μm that is not observed in the active site spectra. The probable reason for this difference is that extinct sinters are dry and active sinters are generally wet, with water in the active sinter deposits suppressing the reflectance peak. ASTER VNIR and SWIR spectroscopy for active and extinct sites was similar and could not easily be discriminated. The active sites had a chlorophyll reflectance peak that the extinct sites locally lacked. But, the broad spectral band passes of ASTER, combined with the 15 and 30 m pixel sizes, made it difficult to discriminate specific materials, and led to the spectral dominance of dry and green vegetation in each pixel. However, the spectra were not pure vegetation. It was evident that there were other materials (i.e. water, chlorophyll, alteration minerals, etc.) that increased the reflectance in the visible green and red, but because the spectra were too broad, other materials could not be specifically identified. Both the ASTER 4/6 and the AVIRIS 139/195 SWIR band ratios proved useful for identifying areas of thermal alteration. Altered rocks always have a ratio greater than unity, which was the case for all field sites at Yellowstone. This confirms that ASTER and AVIRIS band ratioing techniques can effectively detect altered rocks in these geyser basins. In most cases, the extinct sites had a higher alteration ratio than the active sites, provided those sites were not masked by vegetation.

The ASTER thermal infrared region was useful in detecting thermal anomalies of both active and extinct springs. The depth of 9.2 μm emissivity feature is directly related to silica abundance. In general, the extinct springs contained more silica than the active spring sites. Using ASTER TIR imagery, temperatures over the extinct springs were commonly higher or the same as the active springs. Probable reasons for this include cooling winds generated over the active sites during eruptions, masking actual surface temperatures. Also, the extinct sites may have different plumbing system geometries than the active sites, allowing more heat to radiate without the convective heat loss from the water.

The Yellowstone volcanic system is the prime terrestrial analogue for Martian studies, as it has characteristics thought to be present on Mars if the planet ever developed hydrothermal systems. Potential similarities include hot spot volcanism, alkaline to neutral hot spring waters, hydrothermal minerals, including siliceous sinter and iron bearing hydrothermal minerals. If active or extinct hydrothermal systems exist on Mars on a scale similar to or larger than Yellowstone's springs, THEMIS should be able to identify them, providing complications, such as the eolian dust mantle, are limited.

A primary goal of this study was to distinguish between active and extinct hot spring areas. These areas were best identified using field-based VNIR spectroscopy, hyperspectral SWIR spectroscopy, including band ratioing, and multispectral TIR emissivities and temperatures. Multispectral VNIR and SWIR spectroscopy could not easily distinguish active and extinct sites because of broad band passes and larger spatial resolutions. Therefore, based upon the work at Yellowstone as an analog to detect hot springs on Mars, rover-based VNIR spectroscopy, hyperspectral SWIR spectroscopy, multispectral TIR emissivities and temperatures would be most useful; multispectral VNIR and SWIR spectroscopy would probably not be as effective. Also, rover-based SWIR and TIR spectroscopy would be advantageous on Mars, although these instruments were not implemented in this study.

Hyperspectral instruments similar to AVIRIS are being considered for future Mars missions. The NASA Mars Reconnaissance Orbiter (MRO) is scheduled to launch in 2005. MRO will be equipped with a hyperspectral VNIR-SWIR spectrometer (CRISM) from 0.4 to 4.0 μm to study surface composition. Primary objectives include the search for evidence of past or present water. Martian hyperspectral data sets will be extremely important for detailed mineralogical studies of potential hydrothermal systems and would greatly benefit our current knowledge of the red planet.

Acknowledgements

The authors wish to thank the National Park Service and the Yellowstone Research Permit Office, especially Christine Hendrix, Ann Rodman, and Steve Miller, who made this field work possible. Ava Horowitz, Mike Keller, and Rocco Paperiello provided helpful guidance and assistance on the research.

The reviews of Michael Abrams and Steven Anderson greatly improved this manuscript. In addition, William Stefanov provided use of the VNIR field spectrometer, and Robert O. Green and James Granahan provided access to the AVIRIS data and the atmospheric correction software. Research funding for this study has been provided by the NASA Solid Earth and Natural Hazards Program (NAG5-9439) as well as the ASTER science project.

References

Abrams, M.J., Ashley, L., Rowan, L., Goetz, A., Kahle, A., 1977. Mapping of hydrothermal alteration in the Cuprite Mining District, Nevada, using aircraft scanner images for the spectral region 0.46 to 2.36 μm. Geology 5, 713–718.

Bargar, K.E., Fournier, R.O., 1988. Effects of glacial ice on subsurface temperatures of subsurface temperatures of hydrothermal systems in Yellowstone National Park, Wyoming: fluid-inclusion evidence. Geology 16, 1077–1080.

Boynton, W.V., Feldman, W.C., Squyres, S.W., Prettyman, T., Brückner, J., Evans, L.G., Reedy, R.C., Starr, R., Arnold, J.R., Drake, D.M., Englert, P.A.J., Metzger, A.E., Mitrofanov, I., Trombka, J.I., d'Uston, C., Wänke, H., Gasnault, O., Hamara, D.K., Janes, D.M., Marcialis, R.L., Maurice, S., Mikheeva, I., Taylor, G.J., Tokar, R., Shinohara, C., 2002. Distribution of hydrogen in the near-surface of Mars: evidence for sub-surface ice deposits. Science 297, 81–85.

Brock, T.D., 1994. Life at High Temperatures. Yellowstone Association for Natural Science History, and Education, Wyoming. 31 pp.

Bryan, T.S., 1995. The Geysers of Yellowstone, Third Edition. University Press of Colorado, Colorado, 462 pp.

Bryan, T.S., 2000. The Geyser Fields of the World. Yellowstone Interpretive Training Presentation, 12 pp.

Bulmer, M.H., Gregg, T., 1998. Apollinaris Patera: an assessment based on the 2001 landing site evaluation criteria. Mars Surveyor 2001 Landing Site Workshop. NASA Ames-Research Center, Moffett Field, CA, pp. 1–6.

Chesterman, C., 1979. National Audubon Society Field Guide to North American Rocks and Minerals. Alfred A. Knopf, New York, 850 pp.

Christensen, P.R., 2001. The hematite sites. Second Landing Site Workshop for 2003 Mars Exploration Rovers. Pasadena, CA.

Christensen, P.R., Jakosky, B.M., Kieffer, H.H., Malin, M.C., McSween, H.Y., Nealson, K., Mehall, G., Silverman, S., Ferry, S., 1999. The Thermal Emission Imaging System (THEMIS) instrument for the 2001 Orbiter. Lunar Planet. Sci. XXX (1470), 1–2 (abstract).

Christensen, P.R., Bandfield, J.L., Smith, M.D., Hamilton, V.E., Clark, R.N., 2000. Identification of a Basaltic component on the Martian surface from thermal emission spectrometer data. J. Geophys. Res. 105 (E4), 9609–9621.

Christensen, P.R., Clark, R.L., Kieffer, H.H., Malin, M.C., Pearl, J.C., Banfield, J.L., Edgett, K.S., Hamilton, V.E., Hoefen, T., Lane, M.D., Morris, R.V., Pearson, R., Rousch, T., Ruff, S.W., Smith, M.D., 2000. Detection of crystalline hematite mineralization on Mars by the thermal emission spectrometer: evidence for near-surface water. J. Geophys. Res. 105 (E4), 9623–9642.

Christiansen, R.L., 1982. Late Cenozoic volcanism of the Island Park Area, Eastern Idaho. In: Bonnichsen, B., Breckenridge, R.M. (Eds.), Cenozoic Geology of Idaho. Idaho Bureau of Mines and Geology Bulletin, 26, 345–368.

Christiansen, R.L., 1984. Yellowstone magmatic evolution: its bearing on understanding large-volume explosive volcanism. Explosive Volcanism: Inception, Evolution, and Hazards. Studies in Geophysics. National Academy Press, Washington, pp. 84–95.

Clark, R.N., 1993. Mapping minerals with imaging spectroscopy. U.S. Geol. Surv., Off. Miner. Serv. Bull. 2039, 141–150.

Clark, R.N., Swayze, G.A., Gallaghar, A., Gorelick, N., Kruse, F., 1991. Mapping with imaging spectrometer data using the complete band shape least-squares algorithm simultaneously fit to multiple spectral features from multiple materials. AVIRIS Airborne Geoscience Workshop Proceedings 1991. JPL Publication, Pasadena, CA, pp. 1–2.

Dohm, J.M., Baker, V.R., Anderson, R.C., Scott, D.H., Rice Jr., J.W., Hare, T.M., 2000. Identifying Martian hydrothermal sites: geological investigation utilizing multiple datasets. Lunar Planet. Sci. XXXI (1613), 1–2 (abstract, CD-ROM).

Embree, G.F., Hoggan, R.D., 1999. Secondary deformation within the Huckleberry Ridge Tuff and subadjacent pliocene units near the Teton Dam: road log to the regional geology of the eastern margin of the Snake River Plain, Idaho. In: Hughes, S.S, Thackray, G.D. (Eds.), Guidebook to the Geology of Eastern Idaho. Idaho Museum of Natural History, Idaho, pp. 181–202.

Farmer, J.D., 1996. Hydrothermal processes on Mars: an assessment of present evidence. Evolution of Hydrothermal Ecosystems on Earth (and Mars?). Wiley, England, pp. 273–299.

Farmer, J.D., 2000. Hydrothermal systems: doorways to early biosphere evolution. GSA Today 10 (7), 1–11.

Farmer, J.D., DesMarais, D.J., 1999. Exploring for a record of ancient Martian life. J. Geophys. Res. 104 (E11), 26977–26995.

Farmer, J.D., Cady, S., DesMarais, D.J., 1995. Fossilization processes in thermal springs. Abstr Programs-Geol. Soc. Am. 27 (6), 305.

Farmer, J.D., Nelson, D., Greeley, R., Kusmin, R., 2001. Mars 2003: site priorities for astrobiology. First Landing Site Workshop for 2003 Mars Exploration Rovers, no. 9038. NASA Ames-Research Center, Mountain View, CA, pp. 1–2. Abstract.

Fournier, R.O., 1989. Geochemistry and dynamics of the Yellowstone National Park Hydrothermal System. Annu. Rev. Earth Planet. Sci. 17, 13–53.

Fournier, R.O., Pitt, A.M., 1985. The Yellowstone Magmatic-Hydrothermal System. In: Stone, C. (Ed.), Trans.-Geotherm. Resour. Counc., Int. Symp. Geotherm. Energy. Geothermal Resources Council, Davis, CA, pp. 319–327.

Franke, M.A., 2000. Yellowstone in the Afterglow: Lessons From the Fires. National Park Service, Mammoth Hot Springs, Wyoming. YCRNR200003.

Fritz, W.J., 1985. Roadside Geology of the Yellowstone Country. Mountain Press Publishing Company, Montana. 149 pp.

Gillespie, A.R., Kahle, A.B., Palluconi, F.D., 1984. Mapping alluvial fans in Death Valley, California, using multichannel thermal infrared images. Geophys. Res. Lett. 11, 1153–1156.

Green, R.O., Eastwood, M.L., Sarture, C.M., Chrien, T.G., Aronsson, M., Chippendale, B.J., Faust, J.A., Pavri, B.E., Chovit, C.J., Solis, M., Olah, M.R., Williams, Q., 1998. Imaging spectroscopy and the Airborne Visible/Infrared Imaging Spectrometer (AVIRIS). Remote Sens. Environ. 65 (3), 227–248.

Guidry, S.A., Chafetz, H.S., 1999. Preservation of microbes in geyserite and siliceous sinter: Yellowstone National Park, Wyoming. Lunar Planet. Sci. XXX (1152) (Abstract, CD-ROM).

Gulick, V.C., 1998. Potential Mars Surveyor 2001 landing sites near Apollinaris Patera. Mars Surveyor 2001 Landing Site Workshop, no. 9032. NASA Ames-Research Center, Moffett Field, CA, pp. 1–2. Abstract.

Harris, A.G., Tuttle, E., 1975. Geology of National Parks, 4th ed. Kendall/Hunt Publishing Company, Iowa, pp. 480–500.

Hellman, M.J., 2002. Analysis of hot springs in Yellowstone National Park using ASTER and AVIRIS remote sensing, M.S. Thesis, Univ. Pittsburgh, Pittsburgh. 187 pp.

Hellman, M.J., Ramsey, M.S., 2001. Analysis of hot springs in Yellowstone National Park using ASTER and AVIRIS remote sensing. EOS Transactions, AGU, 82:47, Fall Meet. Suppl., F1360.

Hook, S.J., Rast, M., 1990. Mineralogic mapping using Airborne Visible Infrared Imaging Spectrometer (AVIRIS) Shortwave Infrared (SWIR) data acquired over Cuprite, Nevada. AVIRIS Airborne Geoscience Workshop Proceedings 1990. JPL, Pasadena, CA, pp. 199–207.

Hook, S.J., Gabell, A.R., Green, A.A., Kealy, P.S., 1992. A comparison of techniques for extracting emissivity information from thermal infrared data for geologic studies. Remote Sens. Environ. 42, 123–135.

Hook, S.J., Karlstrom, K.E., Miller, C.F., McCaffrey, K.J.W., 1994. Mapping the Piute Mountains, California, with Thermal Infrared Multispectral Scanner (TIMS) images. J. Geophys. Res., 99, 15, 605–615, 622.

Hunt, G.R., 1980. Electromagnetic radiation: the communication link in remote sensing. In: Siegel, B.S, Gillespie, A.R. (Eds.), Remote Sensing in Geology. Wiley, New York, pp. 5–45.

Huntington, J.F., 1996. The role of remote sensing in finding hydrothermal mineral deposits on Earth. Evolution of Hydrothermal Ecosystems on Earth (and Mars?). Wiley, England, pp. 214–234.

Kahle, A.B., 1987. Surface emittance, temperature, and thermal inertia derived from Thermal Infrared Multispectral Scanner (TIMS) data for Death Valley, California. Geophysics 52, 858–874.

Kahle, A.B., Palluconi, F.D., Hook, S.J., Realmuto, V.J., Bothwell, G., 1991. The Advanced Spaceborne Thermal Emission and Reflectance radiometer (ASTER). Int. J. Imaging Syst. Technol. 3, 144–156.

Kokaly, R.F., Clark, R.N., Livo, K.E., 1998. Mapping the biology and mineralogy of Yellowstone National Park using imaging spectroscopy. Summaries of the 7th Annual JPL Airborne Earth Science Workshop. JPL Publication 97–21, vol. 1. JPL, Pasadena, CA, pp. 245–254.

Kruse, F., 1999. Mapping hot spring deposits with AVIRIS at Steamboat Springs, Nevada. AVIRIS Airborne Geoscience Workshop Proceedings 1999. JPL Publication, Pasadena, CA, pp. 1–7.

Lane, M.D., Christensen, P.R., Hartmann, W.K., THEMIS Science Team, 2003. A study of Meridiani Planum, Mars, using THEMIS Data. Sixth International Conference on Mars, Pasadena, CA. Abstract, no. 3122.

Macenka, S.A., Chrisp, M.P., 1987. Airborne Visible/Infrared Imaging Spectrometer (AVIRIS) spectrometer design and performance. JPL Publication 87-38, 13–24.

Marler, G.D., 1964. Studies of Geysers and Hot Springs Along the Firehole River, Yellowstone National Park, Wyoming. Yellowstone Library and Museum Association, pp. 1–49.

Nash, G.D., Johnson, G.W., 2002. Soil mineralogy anomaly detection in Dixie Valley, Nevada using hyperspectral data. Proceedings of the Twenty-Seventh Workshop on Geothermal Reservoir Engineering Stanford University, California, SGP-TR-171.

Nelson, D.M., Farmer, J.D., Greeley, R., Klein, H.P., Kuzmin, R.O., 1998. Geology and landing sites of the Elysium Basin-Terra Cimmeria region, Mars. Mars Surveyor 2001 Landing Site Workshop. NASA Ames-Research Center, Moffett Field, CA, pp. 71–73.

Newsom, H., Barber, C., Thorsos, I., Davies, A., 2003. MER 2003 landing sites—impact crater lake and hydrothermal deposits. 3rd 2003 Mars Exploration Rovers Landing Site Selection Workshop, Pasadena, CA no. 9008, 1–15.

Pieri, D.C., Abrams, M.J., 2004. ASTER watches the world's volcanoes: a new paradigm for volanological observations from orbit. J. Volcanol. Geotherm. Res. 135, 13–28 (this issue).

Porter, W.M., Enmark, H.T., 1987. A system overview of the Airborne Visible/Infrared Imaging Spectrometer (AVIRIS). JPL Publication 87-38, 3–12.

Ramsey, M.S., Dehn, J., 2004. Spaceborne observations of the 2000 Bezymianny, Kamchatka eruption: the integration of high-resolution ASTER data into near real-time monitoring using AVHRR. J. Volcanol. Geotherm. Res. 135, 169–193 (this issue).

Ramsey, M.S., Christensen, P.R., Lancaster, N., Howard, D.A., 1999. Identification of sand sources and transport pathways at the Kelso Dunes, California using thermal infrared remote sensing. Geol. Soc. Am. Bull. 111, 646–662.

Realmuto, V.J., 1990. Separating the effects of temperature and emissivity: emissivity spectrum normalization, proceedings of the second annual Thermal Infrared Multispectral Scanner (TIMS) worshop. In: Abbott, E.A. (Ed.), Proceedings of the Second Thermal Infrared Multispectral Scanner (TIMS) Workshop. JPL Publication, Pasadena, CA, 90-55, pp. 31–36.

Rowan, L.C., Crowley, J.K., Schmidt, R.G., Ager, C.M., Mars, J.C., 2000. Mapping hydrothermally altered rocks by analyzing hyperspectral image (AVIRIS) data of forested areas in the Southeastern United States. J. Geochem. Explor. 68, 145–166.

Ruiz-Armenta, J.R., Prol-Ledesma, R.M., 1998. Techniques for enhancing the spectral response of hydrothermal alteration minerals in thematic mapper images of central Mexico. Int. J. Remote Sens. 19 (10), 1981–2000.

Sabins, F.F., 1999. Remote sensing for mineral exploration. Ore Geol. Rev. 14, 157–183.
Salisbury, J.W., D'Aria, D.M., 1992. Emissivity of terrestrial materials in the 8–14 μm atmospheric window. Remote Sens. Environ. 42, 83–106.
Smith, R.B., Siegel, L.J., 2000. Windows Into the Earth: the Geologic Story of Yellowstone and the Grand National Teton Parks. Oxford Univ. Press, New York, 242 pp.
Sultan, M., Arvidson, R.E., Sturchio, N.C., Guinness, E.A., 1987. Lithologic mapping in Arid regions with Landsat Thematic Mapper data: Meatiq dome, Egypt. Geol. Soc. Am. Bull. 99, 748–762.
Thome, K., Arai, K., Hook, S., Kieffer, H., Lang, H., Matsunaga, T., Ono, A., Palluconi, F., Sakuma, H., Slater, P., Takashima, T., Tonooka, H., Tsuchida, S., Welch, R.M., Zalewski, E., 1998. ASTER preflight and inflight calibration and the validation of level 2 products. IEEE Trans. Geosci. Remote Sens. 36 (4), 1161–1172.
Thorsos, I.E., Newsom, H.E., Davies, A.G., 2002. Impact-induced hydrothermal systems and mineral deposition on Mars. Lunar Planet. Sci. XXXIII (1912) (Abstract, CD-ROM).
Vane, G., Porter, W.M., Reimer, J.H., Chrien, T.G., Green, R.O., 1987. AVIRIS performance during the 1987 flight season: an AVIRIS project assessment and summary of the NASA-sponsored performance evaluation. AVIRIS Airborne Geoscience Workshop Proceedings 1987, pp. 1–20.
Vincent, R.K., 1997. Fundamentals of Geological and Environmental Remote Sensing. Prentice-Hall, New Jersey. 366 pp.
Vincent, R.K., Pleitner, P.K., Wilson, M.L., 1984. Integration of Airborne Thematic Mapper and Thermal Infrared Multispectral Scanner data for lithologic and hydrothermal alteration mapping. Proceedings of the International Symposium on Remote Sensing of the Environment, Third Thematic Conference. Remote Sensing for Exploration Geology, vol. 1. Erim International, Paris, France, pp. 219–226.
Wade, M.L., Agresti, D.G., Wdowiak, T.J., Armendarez, L.P., Farmer, J.D., 1999. A Mössbauer investigation of iron-rich terrestrial hydrothermal vent systems: lessons for Mars exploration. J. Geophys. Res. 104 (E4), 8489–8507.
Walter, M.R., DesMarais, D.J., 1993. Preservation of biological information in thermal spring deposits: developing a strategy for the search for fossil life on Mars. Icarus 101, 129–143.
White, D.E., et al., 1988. The geology and remarkable thermal activity of the Norris Geyser Basin. Prof. Pap.-U.S. Geol. Surv. 1456, 84 pp.
Yamaguchi, Y., Kahle, A.B., Tsu, H., Kawakami, T., Pniel, M., 1998. Overview of the advanced spaceborne thermal emission and reflectance radiometer (ASTER). IEEE Trans. Geosci. Remote Sens. 36, 1062–1071.

Further reading

Instrument Websites:
ASTER Website: http://asterweb.jpl.nasa.gov/
AVIRIS Website: http://malaku.jpl.nasa.gov/aviris.html
TES Website: http://tes.asu.edu/
THEMIS Website: http://themis.la.asu.edu/